Available online at www.sciencedirect.com
SCIENCE DIRECT®
Journal of Computational Physics 190 (2003) 419–458
JOURNAL OF COMPUTATIONAL PHYSICS
www.elsevier.com/locate/jcp

High-order non-uniform grid schemes for numerical simulation of hypersonic boundary-layer stability and transition

Xiaolin Zhong *, Mahidhar Tatineni

Mechanical and Aerospace Engineering Department, University of California, 46-147C, Engineering IV Building, 420 Westwood Plaza, Los Angeles, CA 90095-1597, USA

Received 19 November 2002; received in revised form 12 May 2003; accepted 14 May 2003

Abstract

The direct numerical simulation of receptivity, instability and transition of hypersonic boundary layers requires high-order accurate schemes because lower-order schemes do not have an adequate accuracy level to compute the large range of time and length scales in such flow fields. The main limiting factor in the application of high-order schemes to practical boundary-layer flow problems is the numerical instability of high-order boundary closure schemes on the wall. This paper presents a family of high-order non-uniform grid finite difference schemes with stable boundary closures for the direct numerical simulation of hypersonic boundary-layer transition. By using an appropriate grid stretching, and clustering grid points near the boundary, high-order schemes with stable boundary closures can be obtained. The order of the schemes ranges from first-order at the lowest, to the global spectral collocation method at the highest. The accuracy and stability of the new high-order numerical schemes is tested by numerical simulations of the linear wave equation and two-dimensional incompressible flat plate boundary layer flows. The high-order non-uniform-grid schemes (up to the 11th-order) are subsequently applied for the simulation of the receptivity of a hypersonic boundary layer to free stream disturbances over a blunt leading edge. The steady and unsteady results show that the new high-order schemes are stable and are able to produce high accuracy for computations of the nonlinear two-dimensional Navier–Stokes equations for the wall bounded supersonic flow.

AMS: 65M06; 76M20; 76K05

Keywords: High-order finite difference schemes; Unsteady hypersonic flow simulations; Partial differential equations

1. Introduction

The prediction of laminar-turbulent transition in hypersonic boundary layers is a critical part of the aerodynamic design and control of hypersonic vehicles [1]. The transition process is a result of the nonlinear

* Corresponding author. Tel.: 1-310-825-2905.
E-mail address: xiaolin@seas.ucla.edu (X. Zhong).

0021-9991/$ - see front matter
doi:10.1016/S0021-9991(03)00282-1

response of laminar boundary layers to forcing disturbances [2–5], which can originate from many different sources including free stream disturbances, surface roughness and vibrations [6]. In an environment with weak initial disturbances, the path to transition consists of three stages: (1) receptivity, (2) linear eigenmode growth or transient growth, and (3) nonlinear breakdown to turbulence. The first stage is the receptivity process [7], which converts the environmental disturbances into initial instability waves in the boundary layers. The second stage is the subsequent linear development and growth of boundary-layer instability waves. The third stage is the breakdown of linear instability waves, and the transition to turbulence after the linear instability waves reach certain magnitudes. All these aspects of stability and transition in hypersonic flows are current areas of active research [8–13]. One of the important aspects of supersonic and hypersonic boundary layer transition is the receptivity of hypersonic boundary layers. The study of the receptivity process provides important initial conditions for the instability waves in the boundary layer. Fig. 1 shows a schematic of wave interactions in the leading edge region of a hypersonic flow in the presence of free stream disturbances. The receptivity phenomena are altered considerably by the bow shock in front of the body. The interaction of free stream waves with the shock affects the receptivity process of the boundary layer behind the shock.

Due to the complexity of transient hypersonic flow fields involved in the receptivity process, an effective approach for studying hypersonic boundary layer receptivity, stability and transition is to numerically solve the time-dependent three-dimensional Navier–Stokes equations for the temporally or spatially evolving instability waves. It is necessary to use high-order numerical methods for the simulation in order to resolve the wide range of length and time scales of the complex wave fields in hypersonic boundary layers. Hence, in this regard high-order finite-difference schemes have recently received much attention for the direct numerical simulations of transitional and turbulent flows [14–18]. Finite-difference schemes include both traditional explicit schemes and compact [14] schemes. In [19], Zhong presented and validated a new fifth-order upwind finite difference shock fitting method for the direct numerical simulation of hypersonic flows with a strong bow shock and with stiff source terms. The use of the shock-fitting method makes it possible to accurately compute the physical bow-shock interactions, and the development of instability waves in the boundary layers. The fifth-order shock-fitting schemes were derived on a uniform grid. For a curvilinear stretched grid, typically used in simulations of viscous flow in a boundary layer, the physical coordinates

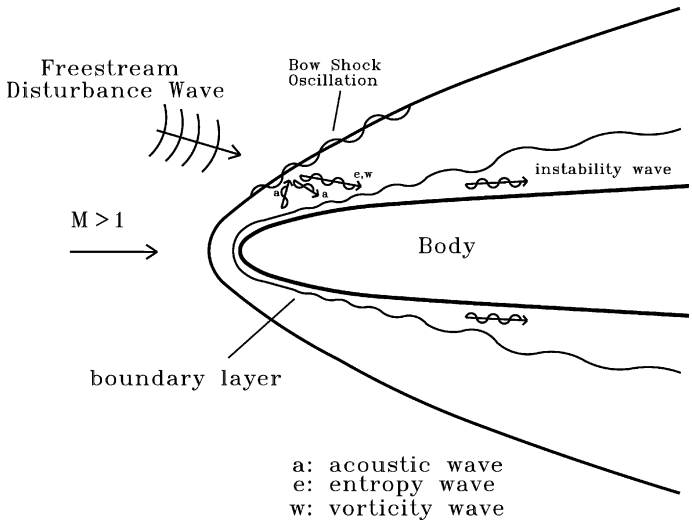

Fig. 1. A schematic of the wave field of the interaction between a bow shock and free-stream disturbances in the leading edge receptivity process.

with a non-uniform grid are first transformed to a uniform grid in the computational coordinates. The high-order schemes are subsequently applied to the transformed equations in a uniform grid. The fifth-order shock-fitting scheme was subsequently used for numerical studies of the receptivity of two-dimensional Mach 15 flows over a blunt leading edge [20].

However, most finite difference schemes used in direct numerical simulation are either central difference schemes [14,15] with filtering or upwind high-order schemes [19,21–23]. One of the main difficulties in applying high-order schemes to practical viscous flow simulations is the numerical instability of boundary closure schemes used on solid wall boundary layer. As a result, in most direct numerical simulations of supersonic and hypersonic boundary-layer flows, the orders of accuracy of numerical methods are often limited due to the numerical instability of the boundary closure schemes. Most high-order explicit and compact finite schemes are derived on a uniformly spaced grid. The schemes are applied to a non-uniform grid by a coordinate transform from the non-uniform physical coordinates to uniform computational coordinate. The finite difference schemes are applied in the uniform computational coordinates through this transformation. The main limiting factor in the application of high-order schemes is the numerical instability of high-order boundary closure schemes [15,24,25]. For example, difference schemes of fourth-order or higher are unstable when they are coupled with high-order boundary schemes using one-sided finite-difference approximations [15,24]. Kreiss and Scherer originally developed a procedure to ensure the stability of numerical closures [26]. Based on this theory, Strand [27] developed finite difference approximations for 'd/dx' which satisfy the summation by parts rule. They derived stable difference operators upto fifth-order accurate at the boundary and sixth-order accurate in the interior. In addition, they determined the parameters such that the bandwith of the operators was minimized. Carpenter et al. [24] showed that for a sixth-order inner compact scheme, only a third-order boundary scheme can be used without introducing instability. This results in globally fourth-order accurate schemes even though the inner scheme is sixth-order accurate. If the order of the schemes is increased further, it is necessary to use much lower order boundary closure scheme in order to maintain numerical stability. As a consequence, the orders of accuracy of numerical methods used in most practical direct numerical simulation studies of compressible and incompressible flows are often limited by the numerical instability of the boundary closure schemes. The overall accuracies of the schemes are at most one order higher than the order of the boundary scheme, no matter how high the order of the interior scheme.

As summarized above, the orders of accuracy of numerical methods used in most current practical direct numerical simulation studies of compressible flows are limited by the numerical instability of the boundary closure schemes. This paper presents a family of simple high-order non-uniform finite-difference schemes with stable boundary closures for the direct numerical simulations of hypersonic boundary layer flows. The main motivation is the application of the high-order schemes to the direct numerical simulations of the receptivity, stability, and transition of hypersonic boundary layers. Using the new schemes the instability of the boundary closures can be overcome for arbitrarily high-order finite difference schemes in the interior and at the boundaries. The schemes are derived directly on a non-uniform stretched grid without coordinate transformation to a uniform grid. The coefficients of the high-order schemes are determined based on polynomial interpolation in the non-uniform grid computational domain. The amount of grid stretching is determined to maintain the stability of the overall schemes. Explicit formulas are presented for computing the coefficients for arbitrary order explicit and compact schemes on a general non-uniform grid. As a result, the high-order schemes can be easily used in applications by computing the derivative coefficients using these explicit formulas.

The new high-order (up to 16th-order) schemes are first tested in computing a linear wave equation with time oscillatory boundary conditions. The scheme was further tested by computing two-dimensional incompressible boundary layer flows over a flat plate based on the full nonlinear Navier–Stokes equations. The high-order finite difference schemes with stable boundary closures are then applied to the direct numerical simulation studies of the receptivity of Mach 15 boundary layers over a blunt leading edge.

2. Governing equations

The governing equations for the direct numerical simulations of hypersonic viscous flows are the unsteady two or three-dimensional Navier–Stokes equations written in the following conservation-law form:

$$\frac{\partial U^*}{\partial t^*} + \frac{\partial F_j^*}{\partial x_j^*} + \frac{\partial F_{vj}^*}{\partial x_j^*} = 0, \tag{1}$$

where superscript "$*$" represents dimensional variables, and t^* and x_j^* are independent variables of Cartesian coordinates and time, respectively. The vector of the conservative flow variables is

$$U^* = \{\rho^*, \rho^* u_1^*, \rho^* u_2^*, \rho^* u_3^*, e^*\}. \tag{2}$$

The gas is assumed to be thermally and calorically perfect. The equations of states are

$$p^* = \rho^* R^* T^*, \tag{3}$$

$$e^* = \rho^* \left(c_{\mathrm{v}}^* T^* + \frac{\rho^*}{2} u_k^* u_k^* \right), \tag{4}$$

where the gas constant R^* and the specific heats c_{p}^* and c_{v}^* are assumed to be constants with a given ratio of specific heats γ. The flux vectors in Eq. (1) are

$$F_j^* = \begin{Bmatrix} \rho^* u_j^* \\ \rho^* u_1^* u_j^* + p^* \delta_{1j} \\ \rho^* u_2^* u_j^* + p^* \delta_{2j} \\ \rho^* u_3^* u_j^* + p^* \delta_{3j} \\ (e^* + p^*) u_j^* \end{Bmatrix}, \tag{5}$$

$$F_{vj}^* = \begin{Bmatrix} 0 \\ -\tau_{1j}^* \\ -\tau_{2j}^* \\ -\tau_{3j}^* \\ -\tau_{jk}^* u_k^* - q_j^* \end{Bmatrix}, \tag{6}$$

where the viscous stress tensor and heat flux vector are

$$\tau_{ij}^* = \mu^* \left(\frac{\partial u_i^*}{\partial x_j^*} + \frac{\partial u_j^*}{\partial x_i^*} \right) - \frac{2}{3} \mu^* \frac{\partial u_k^*}{\partial x_k^*} \delta_{ij}, \tag{7}$$

$$q_j^* = -\kappa^* \frac{\partial T^*}{\partial x_j^*}, \tag{8}$$

where μ^* is the viscosity coefficient determined by the Sutherland's law,

$$\mu^* = \mu_r^* \left(\frac{T^*}{T_r^*} \right)^{3/2} \frac{T_r^* + T_s^*}{T^* + T_s^*}, \tag{9}$$

and κ^* is the heat conductivity coefficient determined by assuming a constant Prandtl number Pr.

2.1. Boundary conditions

In the leading edge receptivity problem, both steady and unsteady flow solutions of the Navier–Stokes equations are computed by numerical simulations. For a steady flow simulation, flow variables at the supersonic free stream in front of the bow shock are constant. On the other hand, free stream flow variables for an unsteady flow simulation are time varying acoustic wave fields. The body surface is assumed to be a non-slip isothermal wall with a given temperature T_w^*. The pressure at the wall is determined using a characteristic based boundary condition. The bow shock is assumed to be an infinitely thin moving discontinuity surface, where flow variables across the shock are governed by the Rankine–Hugoniot conditions. Using the Rankine–Hugoniot relations jump conditions for flow variables are derived as functions of the free stream flow variables and the local shock normal velocity. The local shock normal velocity is determined by a characteristic compatability equation immediately behind the shock. The detail of the shock fitting formulas can be found in Zhong [19].

3. Coordinate mapping in shock fitting simulations

In the following sections details of the numerical methods are presented. The schemes presented are for two dimensional equations. They can be easily extended for three dimensional flows. In the numerical simulation for the hypersonic flow over a blunt leading edge, the simulations are carried out using a high-order non-uniform grid scheme with a shock fitting treatment for the bow shock. The location and the unsteady movement of the bow shock is an unknown to be solved with the flow variables using the shock-fitting method. The computational domain for a shock-fitting method used in computing steady and unsteady 2-D viscous hypersonic flow over blunt bodies is shown in Fig. 2. Body fitted grids are used in the computations where the oscillating bow shock is treated as an outer computational boundary. Before discretizing the governing equation by a finite difference method, the governing Eq. (1) in the Cartesian coordinates in the body-fitted physical domain are transformed to the rectangular computational domain, bounded by the bow shock and the body surface, by a coordinate transformation. The governing equations

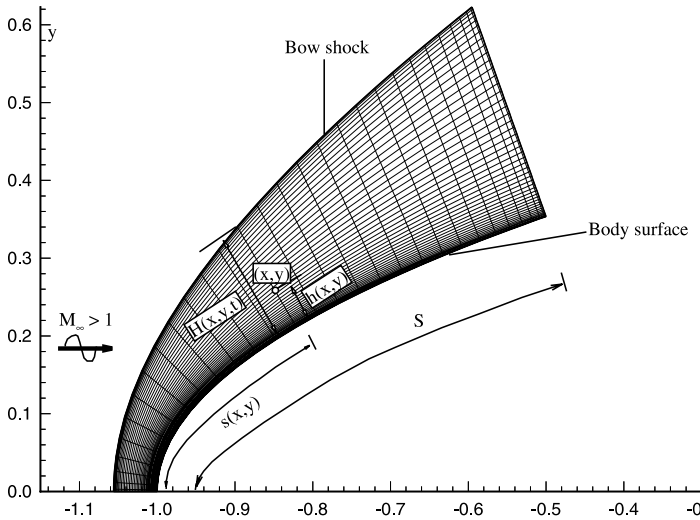

Fig. 2. Computational grid for hypersonic flow over a blunt leading edge where the bow shock shape is obtained as the numerical solution for the upper grid line boundary.

are solved in a general curvilinear coordinates (ξ, η, τ) along body fitted grid lines. During the computations, the grid surface of $\eta =$ constant is unsteady due to the shock movement, but the grid surfaces of $\xi =$ constant are fixed during the calculations.

The specific coordinate transformation for the computational domain shown in Fig. 2 is described as follows. For viscous flow simulations, the physical computational domain between the bow shock and the body is mapped to a square in two steps: (1) (x, y, t) to (X, Y, τ), and (2) (X, Y, τ) to (ξ, η, τ), following Kopriva [28].

In the first step of the transformation, the physical space is mapped to a square in the intermediate coordinate space (X, Y) by the following relation:

$$\begin{cases} X = \frac{2s(x,y)}{S} - 1, \\ Y = \frac{2h(x,y)}{H(x,y,t)} - 1, \end{cases} \tag{10}$$

where s is the local surface curve length, S is total surface curve length in the computational domain, h is the local normal distance of point (x, y) to the body surface, and H is the local shock height. For unsteady flow, $H(x, y, t)$, which is a function of time because of the shock motion, is solved as a dependent variable as shown in Fig. 2. The transformation given by Eq. (10) maps the physical domain to a square domain in (X, Y) space in $[-1, 1] \times [-1, 1]$.

In the second step of the transformation, the (X, Y) space is mapped to a square in (ξ, η) space in order to introduce more grid points near the wall to better resolve the boundary layer structure for a viscous flow simulation. In this paper, a hyperbolic tangent stretching is used in the wall-normal direction as follows:

$$\begin{cases} X = \xi, \\ Y = 2\frac{[1-\tanh(\sigma)]^{\frac{\eta+1}{2}}}{1-\tanh(\sigma^{\frac{\eta+1}{2}})} - 1, \end{cases} \tag{11}$$

where σ is the stretching parameter. The value of σ is chosen to be 0.75 for the simulations presented in this paper. This combined transformation maps the physical domain in (x, y) between the bow shock and the body into a square domain in $(\xi, \eta) \in [-1, 1] \times [-1, 1]$ by the following general relations:

$$\begin{cases} \xi = \xi(x, y), \\ \eta = \eta(x, y, t), \\ \tau = t, \end{cases} \tag{12}$$

where η is a function of t as a result of the unsteady motion of the bow shock induced by free stream disturbances.

The governing Eq. (1) are transformed into the computational domain (ξ, η, τ) as follows:

$$\frac{1}{J}\frac{\partial U}{\partial \tau} + \frac{\partial E'}{\partial \xi} + \frac{\partial F'}{\partial \eta} + \frac{\partial E'_{\mathrm{v}}}{\partial \xi} + \frac{\partial F'_{\mathrm{v}}}{\partial \eta} + U\frac{\partial (1/J)}{\partial \tau} = \frac{W}{J}, \tag{13}$$

where

$$E' = \frac{F_1 \xi_x + F_2 \xi_y}{J}, \tag{14}$$

$$F' = \frac{F_1 \eta_x + F_2 \eta_y + U\eta_t}{J}, \tag{15}$$

$$E'_{\mathrm{v}} = \frac{F_{v1} \xi_x + F_{v2} \xi_y}{J}, \tag{16}$$

$$F'_{\mathrm{v}} = \frac{F_{v1}\eta_x + F_{v2}\eta_y}{J}, \tag{17}$$

$$J = x_\xi y_\eta - x_\eta y_\xi, \tag{18}$$

where J is the Jacobian of the coordinate transformation, and ξ_x, ξ_y, η_x, η_y, and η_t are the grid transformation metrics, which can be computed once the shape of the computational domain is known. The grid metrics can be computed using a simple chain rule using the (ξ, η, τ) to (X, Y, τ), and (X, Y, τ) to (x, y, t) transformations. The derivatives in the (ξ, η) space can be calculated using the stretched grid finite difference formulas presented in Eqs. (30) and (41). It should be noted that the grids in the computational domain will not be uniform, but in fact are stretched (for stability purposes) according to Eq. (26).

The height of the bow shock $H(x, y, t)$ and the time rate of the change of the shock height $H_\tau(x, y, t)$ are governed by shock fitting formulas presented in [19]. The equations for the acceleration and the velocity of the bow shock can be written in the following forms:

$$\frac{\partial H_\tau}{\partial \tau} = f(U_s,\ \partial U_s/\partial\tau,\ U_\infty,\ \partial U_\infty/\partial\tau,\ H,\ H_\tau), \tag{19}$$

$$\frac{\partial H}{\partial \tau} = H_\tau, \tag{20}$$

where subscript s represents flow variables located immediately behind the shock, and subscript ∞ represents flow variables located immediately on the free stream side of the shock. The above formulas can be derived by combining the Rankine–Hugoniot shock relations and a characteristic compatibility relation behind the shock. The detailed formula for the function f in the equations above can be found in [19]. These two equations are additional governing equations for the shock normal velocity and the shock shape.

The spatial derivatives in the transformed governing Eq. (13) for the interior flow variables U and the governing Eqs. (19) and (20) for the bow shock are discretized using the non-uniform grid high-order schemes together with stable boundary closures described in this paper. The inviscid flux terms are discretized using an upwind scheme. For the inviscid flux vectors, the flux Jacobians contain both positive and negative eigenvalues, a simple local Lax–Friedrichs scheme is used to split the inviscid flux vectors into positive and negative wave fields. For example, the flux term F' in Eq. (13) can be split into two terms of pure positive and negative eigenvalues as follows:

$$F' = F'_+ + F'_-, \tag{21}$$

where $F'_+ = (1/2)(F' + \lambda U)$ and $F'_- = (1/2)(F' - \lambda U)$ and λ is chosen to be larger than the local maximum eigenvalue of F'

$$\lambda = \frac{|\nabla\eta|}{J}\left(\sqrt{(\epsilon c)^2 + u'^2} + c\right), \tag{22}$$

where c is the local speed of sound, and

$$u' = \frac{\eta_x u + \eta_y v + \eta_t}{|\nabla\eta|}. \tag{23}$$

The parameter ϵ is a small positive constant added to adjust the smoothness of the splitting. The fluxes F'_+ and F'_- contain only positive and negative eigenvalues, respectively. Therefore, in the spatial discretization of Eq. (13), the derivative of the flux F is split into two terms

$$\frac{\partial F'}{\partial \eta} = \frac{\partial F'_+}{\partial \eta} + \frac{\partial F'_-}{\partial \eta}, \tag{24}$$

where the first term on the right-hand side is discretized by the upwind scheme and the second term by the downwind scheme. The stencil for the upwind or downwind schemes is chosen by biasing the stencil by one point in the appropriate direction. The details of the discretization are given in the next section.

The spatially discretized equations form a system of first-order ordinary differential equations, which are integrated in time using an explicit third-order Runge–Kutta scheme. The shock variables H and H_τ are integrated in time simultaneously with the interior flow variables U. During the time integration of the flow variables, the grid locations and the transformation metrics are function of $H(x, y, t)$ and $H_\tau(x, y, t)$. As a result, at the end of the computations of each stage of the time step, the grids and transformation metrics are recalculated according to the new values of $H(x, y, t)$ and $H_\tau(x, y, t)$.

4. High-order non-uniform grid schemes with boundary closure

The spatial derivatives, such as $\partial E'/\partial \xi$ and $\partial F'/\partial \eta$, in the governing Eq. (13) in (ξ, η) space for the interior flow variables U are discretized by a non-uniform grid high-order schemes together with boundary closure schemes in the square computational domain in (ξ, η) space in $[-1, 1] \times [-1, 1]$. The derivatives are calculated based on a non-uniform grid in the (ξ, η) computational domain. In this paper, the non-uniform grid used for the calculating the derivatives is given by the following stretching function [29]:

$$\xi_i = \frac{\sin^{-1}(-\alpha \cos(\pi i/N))}{\sin^{-1} \alpha}, \tag{25}$$

$$\eta_j = \frac{\sin^{-1}(-\alpha \cos(\pi j/M))}{\sin^{-1} \alpha}, \tag{26}$$

where the parameter α is a positive parameter, which is used to change the stretching of the grid points, i and j are grid index numbers, N and M are the total number of grid points in i and j directions. The high-order non-uniform grid scheme applies a finite difference approximation directly to the grid points in the (ξ, η) space to get the derivatives required in the computational space of the governing Eqs. (19) and (20).

In this section the numerical method is detailed and analyzed by application to the discretization of $\partial u/\partial x$ and $\partial^2 u/\partial x^2$ in a one-dimensional domain of $[-1, 1]$. The application to the two-dimensional square domain in the (ξ, η) space is straightforward. A high-order finite difference scheme is based on a polynomial interpolation of increasing degrees to approximate the derivatives of a function. A compact scheme can be derived by a Hermite polynomial interpolation using both the function values and their derivatives. It is well known (the Runge phenomena) that a high-order polynomial interpolation based on a uniform grid distribution may develop oscillations near the boundary of the interpolation domain. Higher order polynomials lead to larger oscillations at the boundary. Because finite difference schemes are based on polynomial interpolation, it is not surprising that a high-order finite difference scheme based on uniform grids may develop instability due to the boundary closure schemes. On the other hand, a spectral collocation method using the Chebyshev polynomials is identical to a global high-order finite difference scheme using all grid points directly derived on non-uniform grid points located at the zeros or maximas of the Chebyshev polynomials. The Chebyshev grid spacing is as follows:

$$y = \cos(\pi i/N), \tag{27}$$

where i is grid index, N is total number of grid points, and y is the physical coordinate. Therefore, a Chebyshev spectral collocation method using 101 grid points is a 100th-order finite difference scheme

using a grid stretching given by Eq. (27). Such a finite difference scheme is based on a polynomial interpolation on a non-uniform grid distribution without coordinate transformation. Such interpolation is stable both in the interior and in the boundary points because of the condensation of grid points at the boundary. As a result, a 100th-order or higher finite difference scheme based on Chebyshev grid spacing is numerically stable because of the grid stretching at the boundary in the polynomial interpolations. On the other hand, although they are much superior in numerical accuracy, the spectral methods have the drawback that they are computationally expensive because they are global schemes based on all grid points. Such global accuracy may not be necessary in terms of accuracy in many simulations. In addition, the grid spacing given by Eq. (27) leads to a highly stretched grid at the wall when a large number of grid points are used. The minimum grid spacing at the wall is $O(1/N^2)$. Such fine grid spacing leads to a very restrictive stability requirement on the time step in the temporal integration of the equations [30].

Therefore, for the direct numerical simulations of hypersonic wall-bounded flows, an intermediate approach is used to discretize the spatial derivatives using fixed high-order (up to 10–15th-order) local schemes. Grid stretching is used to ensure the stability of boundary closure schemes. At the same time, because the order of the schemes is fixed, the grid stretching at the wall does not need to be as condensed as the full stencil spectral stretching given by Eq. (27). The minimum grid spacing at the wall can be determined so that the high-order schemes are stable with boundary closure. In this paper we show that the minimum grid spacing required for a stable scheme can be of $O(1/N)$, as opposed to the spacing of $O(1/N^2)$ required for full stencil spectral methods. As a result we can have a very high order numerical scheme and maintain a reasonable spacing near the boundaries.

Coefficients for explicit and compact nonuniform grid schemes

The application of high-order schemes on non-uniform grids does not introduce additional computational difficulty in terms of numerical scheme complexity and cost. The coefficients of the high-order schemes at each grid point are different because of grid stretching, but they can be computed and saved in memory once and for all at the beginning of a calculation. The conventional methods for deriving the coefficients for the finite difference (especially the compact) schemes is to use the method of undetermined coefficients with Taylor expansions. The coefficients are computed by solving a linear equation for the coefficients. Such methods are not convenient for deriving the coefficients with non-uniform grids because every case may have a different grid spacing. In addition, the matrix in solving the coefficients has high condition numbers, which can lead to large round off errors in solving the linear equations for the coefficients of the high-order schemes. Therefore, we present explicit formulas for computing the coefficients of the explicit and compact higher order schemes for an arbitrary non-uniform grid distribution.

The derivation for the coefficients for the explicit high order schemes on non-uniform grids is straightforward. They are listed here for completeness. The coefficients are derived from a Lagrange polynomial interpolation. For the case of n grid stencil with arbitrary distribution of grid points with coordinates x_i, the $n-1$ degree interpolation polynomial is:

$$P_n(x) = \sum_{j=1}^{n} l_j(x)\, u_j, \tag{28}$$

where u_j are the variable values at the node points, and

$$l_j(x) = \prod_{l=1, l\neq j}^{n} (x - x_l) \Bigg/ \prod_{l=1, l\neq j}^{n} (x_j - x_l). \tag{29}$$

The derivative at a grid point x_i can be calculated by differentiating the above polynomial as:

$$u_i' = \sum_{j=1}^{n} b_{i,j} u_j, \tag{30}$$

where the coefficients $b_{i,j}$ in the derivatives are different for different grid points with index i, and are given by

$$b_{i,j} = l_j'(x_i). \tag{31}$$

Hence, once the x_i locations of the stencil are given, the coefficients for the finite difference formulas for a high-order scheme in a non-uniform grid can be calculated explicitly using the above formulas. The coefficients for the boundary closure scheme are derived using the same formula and by specifying one-sided grid stencils. The derivatives at all grid points, including the interior and boundary points, can be combined into the following vector formula:

$$\boldsymbol{u}' = \boldsymbol{A}\boldsymbol{u}, \tag{32}$$

where $\boldsymbol{u}$ is a vector of variables and $\boldsymbol{A}$ is a banded coefficients matrix, which can be computed once and for all at the beginning of a calculation.

The explicit formulas for computing the coefficients of a compact scheme in arbitrary non-uniform grids are derived in this paper by generalizing the Hermite interpolation polynomial. Consider a generalized Hermite polynomial interpolation to compute u_0' by interpolation through two groups of grid points: (1) interpolates through both u_i and u_i' for n grid points located at x_i for $(i = 1, \ldots, n)$, and (2) interpolates through only u_i for additional $m + 1$ grid points located at x_j for $(j = 0, -1, \ldots, -m)$. The locations of these node points do not have to be arranged in a particular order, as long as they are distinct points.

The generalized Hermite interpolation polynomial is:

$$\bar{H}(x) = H_n(x) + \sum_{j=0}^{-m} \phi_j(x) d_j. \tag{33}$$

$H_n(x)$ is the Hermite interpolant for the first group of n grid points without x_0:

$$H_n(x) = \sum_{i=1}^{n} u_i h_i(x) + \sum_{i=1}^{n} u_i' \widetilde{h}_i(x), \tag{34}$$

where

$$h_i(x) = \left[1 - 2l_i'(x_i)(x - x_i)\right] l_i^2(x), \tag{35}$$

$$\widetilde{h}_i(x) = (x - x_i) l_i^2(x). \tag{36}$$

The function $\phi_j(x)$ is defined as:

$$\phi_j(x) = (\xi_j(x))^2 l_j(x), \tag{37}$$

where

$$\xi_j(x) = \prod_{l=1}^{n} \frac{x - x_l}{x_j - x_l}. \tag{38}$$

The values of d_j are determined so that the polynomial interpolates through the second group of $m + 1$ grid points (including x_0). There are $m + 1$ conditions for solving for d_j:

$$\bar{H}(x_j) = u_j, \quad j = 0, -1, \ldots, -m. \tag{39}$$

The d_j values are substituted back into the original interpolation polynomial. The formula for the compact derivatives can be derived by evaluating

$$u'_0 = \bar{H}'_n(x_0). \tag{40}$$

This formula leads to the compact coefficients as follows:

$$\sum_{i=0}^{n} b_i u'_i = \sum_{i=0}^{n} a_i u_i + \sum_{j=0}^{-m} c_j u_j, \tag{41}$$

where the coefficients a_i, b_i, and c_j are determined by

$$b_0 = 1, \tag{42}$$

$$b_i = -\left[\widetilde{h_i}'(x_0) - \sum_{j=0}^{-m} \widetilde{h_i}(x_j)\phi'_j(x_0)\right], \tag{43}$$

$$a_i = +\left[h'_i(x_0) - \sum_{j=0}^{-m} h_i(x_j)\phi'_j(x_0)\right], \tag{44}$$

$$c_j = \phi'_j(x_0). \tag{45}$$

It is easy to test that the formulas above lead to the same compact scheme formulas on a uniform grid. For example, a sixth-order compact scheme can be derived using the above formulas with a 5-3 stencil as follows:

$$\frac{1}{3}\, u'_{i-1} + \, u'_i + \frac{1}{3}\, u'_{i+1} = \frac{1}{180h}(5\, u_{i+2} + 140\, u_{i+1} - 140\, u_{i-1} - 5\, u_{i-2}), \tag{46}$$

which is the standard sixth-order compact scheme on a uniform grid [14].

Hence, given the grid distribution, the compact scheme coefficients can be calculated explicitly without using the Taylor expansion for uniform or non-uniform grids. The coefficients at the boundary closure scheme are derived using the same formula by specifying one-sided grid stencils. Similarly, the derivatives at all grid points, including the interior and boundary points, can be combined into the following vector formula:

$$\boldsymbol{P}\boldsymbol{u}' = \boldsymbol{Q}\boldsymbol{u}, \tag{47}$$

where $\boldsymbol{P}$ and $\boldsymbol{Q}$ are banded coefficients matrices, which can be computed once and for all at the beginning of a calculation. In the stability analysis, the compact scheme can also be written into explicit form as

$$\boldsymbol{u}' = \boldsymbol{A}\boldsymbol{u}, \tag{48}$$

where $\boldsymbol{A} = \boldsymbol{P}^{-1}\boldsymbol{Q}$.

Examples of these coefficients' matrix for high-order compact schemes on non-uniform grids are shown in Appendix A. Once the coefficients are computed, the higher-order explicit or compact schemes can be used to discretize a first-order derivative in numerical simulation by using the formulas given by Eqs. (32) or (47). The matrix multiplication is only partially carried because $\boldsymbol{P}$ and $\boldsymbol{Q}$ are banded matrices. Similar

methods can be used to derive explicit formulas for compact schemes to calculate second derivatives on non-uniform grids. They are not presented here.

4.1. Grid spacing

The stability of high-order schemes is dependent on the grid clustering near the boundaries. Spectral collocation methods utilizing the Chebyshev spacing are stable for arbitrary order schemes with boundary closure. The Chebyshev grid spacing is given by Eq. (27). However, this spacing is very restrictive on the time step ($O(1/N^2)$) in a temporal integration of a PDE. In this paper we are using a less restrictive spacing with high-order finite difference schemes in order to maintain stability and high spatial accuracy and an $O(1/N)$ in minimum grid spacing and time step. No attempt is made to search for the optimal grid spacing in terms of stability and accuracy. The stretching used in the paper can vary the grid clustering near the boundaries and hence can be used to prove that stable high-order schemes can be constructed by sufficiently increasing grid clustering near the boundaries.

In this paper, the grid spacing in the numerical simulations is controlled using the stretching function proposed by Kosloff and Tal-Ezer [29] for a spectral method, i.e.,

$$x = \frac{\sin^{-1}(-\alpha\cos(\pi i/N))}{\sin^{-1}\alpha}, \tag{49}$$

where the parameter α is used to change the stretching of the grid points from one limit of a Chebyshev grid at $\alpha \to 0$ and the other limit of an uniform grid at $\alpha = 1$. Hence, the stretching can be controlled to find the optimum α for which the high order scheme is stable.

4.2. Asymptotic stability analysis

The asymptotic stability of the high-order explicit and compact schemes with boundary closures is analyzed by computing the eigenvalues of the matrices obtained by spatial discretization of the following wave equation:

$$\frac{\partial u}{\partial t} + c\frac{\partial u}{\partial x} = 0 \tag{50}$$

in a fixed computational domain $(-1, 1)$. The non-periodic boundary condition is specified at $x = -1$ to a fixed value $u(x = 1, t) = f(t)$. After a computational grid has been assigned to the domain, the spatial derivatives of all grid points, including the interior and boundary points, are discretized by a explicit or compact finite difference algorithms given by Eqs. (32) or (47). Substituting the approximation above into the wave equation (50) with the non-periodic boundary condition at $x = -1$ leads to

$$\frac{\mathrm{d}\boldsymbol{u}}{\mathrm{d}t} = c\boldsymbol{M}\boldsymbol{u} + \boldsymbol{g}(t). \tag{51}$$

The asymptotic stability condition for the semi-discrete equations is that all eigenvalues of matrix $\boldsymbol{M}$ contains no positive real parts.

The asymptotic stability, which requires that the eigenvalues of the spatial discretization matrices contain no positive real parts, is necessary for the stability of long-time integration of the equation. This is a necessary condition for the stability of the schemes when the matrices do not have full sets of eigenvalues and eigenfunctions. Numerical computations show that the matrices for high-order upwind schemes with boundary conditions have full eigenvalues. For such normal matrices, the eigenvalue analysis is accurate in assessing the stability of high-order finite-difference schemes.

In this paper we define the order of a scheme on non-uniform grids to be the same as the degree of polynomial used for interpolation. Fig. 3 (top) shows the spectrum for a sixth-order scheme on a uniform grid of 101 points. The grid stencil in the interior is to use seven points to evaluate the derivative at the center node point, and use a one-sided seven point stencil for the boundary closure scheme. The figure

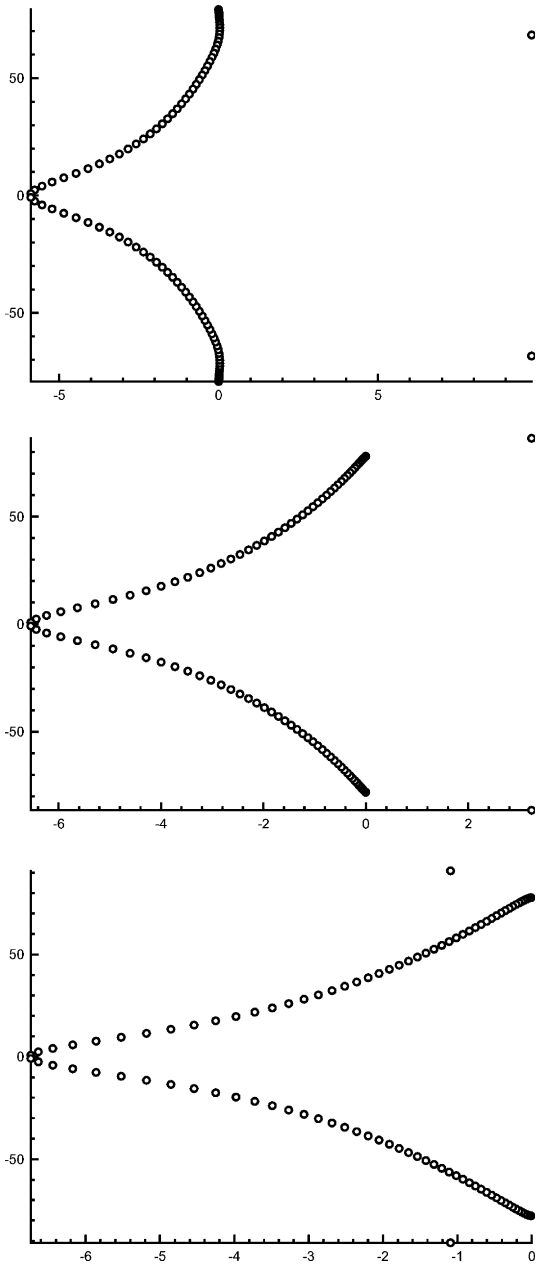

Fig. 3. Eigenvalue spectrum of the spatial discretization matrix for the sixth-order scheme on (top) a uniform grid of 101 points (center) a stretched grid of 101 points with $\alpha = 0.9997$, and (bottom) a stretched grid of 101 points with $\alpha = 0.9995$.

shows that there are two eigenvalues in the unstable region of the spectrum. Therefore a sixth-order scheme with a sixth-order boundary closure scheme will not be stable because a uniform grid is used.

In order to stabilize the sixth-order scheme, a stretched grid given by Eq. (26) is used for the seven point stencil scheme in the physical domain. It is found that the stability of the scheme improves as the grid becomes more and more stretched towards the boundary by decreasing the value of α. Fig. 3 (center) and Fig. 3 (bottom) show the spectrum for the sixth-order scheme on a stretched grid with $\alpha = 0.9997$ and $\alpha = 0.9995$, respectively. The two unstable eigenvalues become less unstable for $\alpha = 0.9997$ and are completely stable for $\alpha = 0.9995$. Hence, computing the derivatives directly on a stretched grid results in a stable boundary closure.

It is also found that as the order increases, the amount of grid stretching needs to be increased in order to stabilize the schemes with boundary closure. Therefore, it is necessary to determine the grid stretching

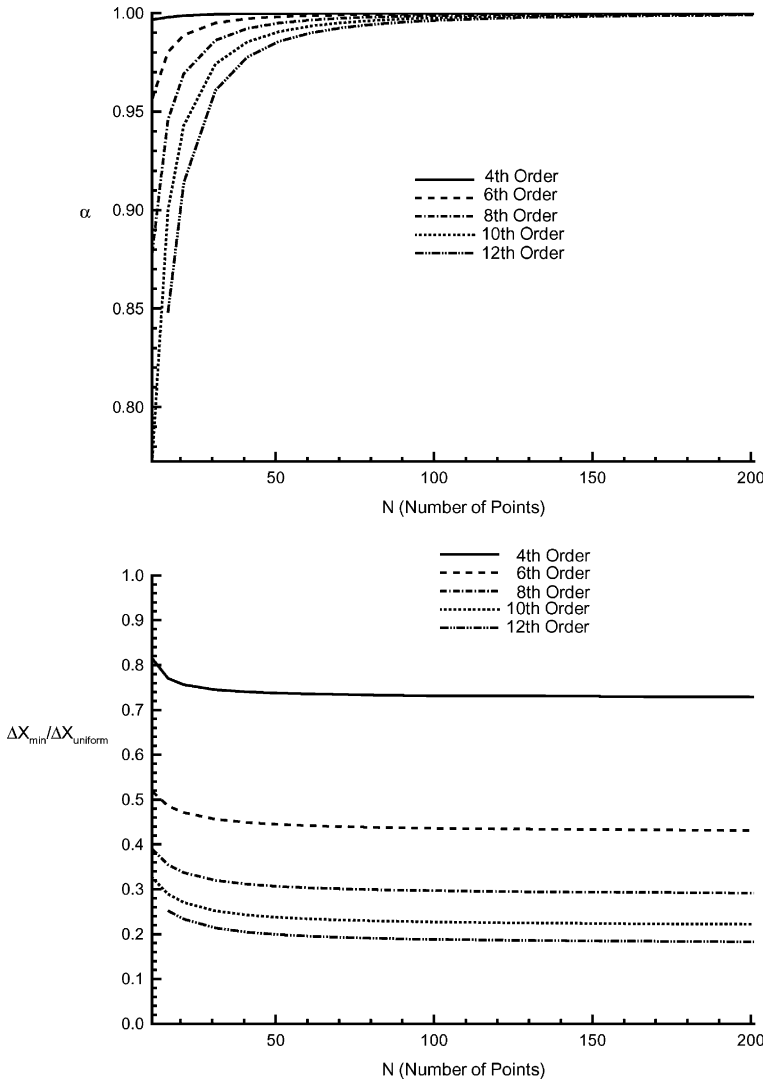

Fig. 4. Top: Variation of grid stretching parameter α required for stable boundary closure, with the total points used, for various schemes. Bottom: Variation of minimum Δx required for stable boundary closure with the total points used, for various schemes.

needed for stable algorithms as a function of the order of the finite difference algorithm and the number of total grid points in the domain. The stability results for the fourth-, sixth-, eighth, 10th-, and 12th-order schemes are presented in Fig. 4. The limits of the grid stretching parameter α and the corresponding minimum $\Delta x_{\min}$ required for a stable closure is plotted versus the total number of points, for all schemes. The $\Delta x_{\min}$ is normalized by averaged grid spacing $\Delta x_{\text{uniform}} = 2/N$. The results show that higher-order schemes required smaller $\Delta x_{\min}$ in order to maintain stable boundary closure. As N increases, the value of $\Delta x_{\min}/\Delta x_{\text{uniform}}$ approaches a constant value, which means that the required minimum grid spacing is of the order of $1/N$. Hence, the grid spacing requirements for stabilizing the new high order schemes are less restrictive than spectral methods (where the $\Delta x_{\min}$ is of order $1/N^2$).

The variation of minimum required grid spacing $\Delta x_{\min}$ for stability with the order of accuracy (stencil width) is shown in Fig. 5. The figure shows that for 6th to 20th-order schemes, $\Delta x_{\min}$ is approximately of $O(1/(NM))$ for a finite difference scheme using a local stencil width of M ($M-1$th-order scheme). This is much less restrictive than the $O(1/N^2)$ spacing in the case of the spectral collocation method based on Chebyshev polynomial. However, it should be noted that unstretching of the order similar to our method can be achieved in spectral element methods where the stencil does not involve the whole domain.

As stated earlier, the instability of the boundary closure scheme is a result of oscillation of polynomial interpolation at the boundary on a uniform grid. It is can also be demonstrated by the distribution in the interpolation error formula given by Eq. (52), where the error is proportional to the following function:

$$g(x) = (x - x_0)(x - x_1)\cdots(x - x_n). \tag{52}$$

The error in approximating the derivative at a grid points x_i is given by $g'(x_0)$.

Fig. 6 shows the distribution of the error function given by Eq. (52) (normalized by the maximum uniform grid truncation error) for a sixth-order scheme on a Chebyshev spacing and two intermediate stretching cases. The truncation error is oscillatory near the boundary for the intermediate stretching cases. This is clearly seen in Fig. 6 (bottom figure) which is a zoomed version of Fig. 6 (top figure). When the stretching is moved closer to the uniform case the oscillations are larger in magnitude and can result in an unstable scheme. Hence, for a stable closure the truncation error near the boundaries must be kept low.

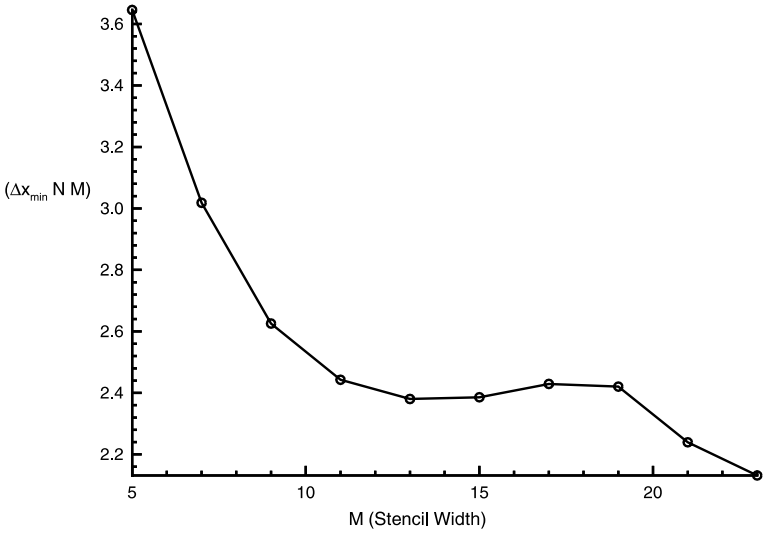

Fig. 5. Variation of minimum Δx required for stable boundary closure with the stencil width, for various schemes.

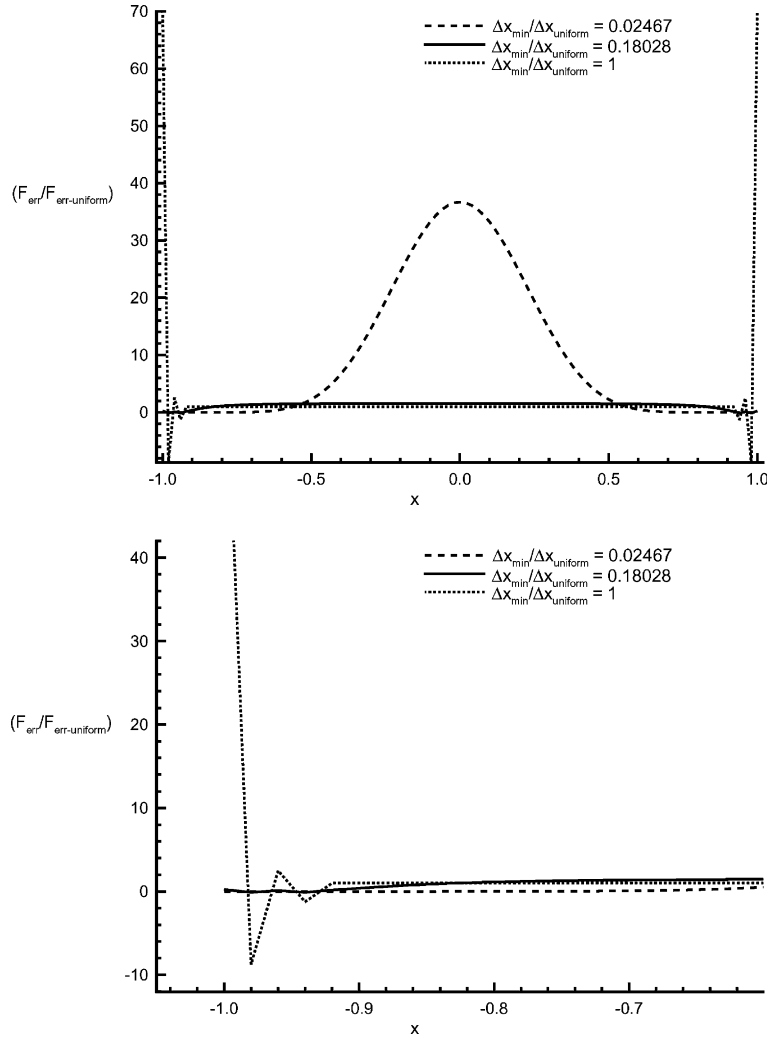

Fig. 6. Distribution of the truncation error (normalized by the maximum uniform grid truncation error) for a sixth-order scheme for 101 points. The error distribution near the boundary is zoomed and shown in the bottom figure.

The stability analysis was repeated for compact schemes with similar results. We tested four cases of compact schemes with a 5–3 (seventh-order), 7–3 (ninth-order), 7–5 (11th-order), and 9–3 (12th-order) grid stencil. An example of the derivative matrix of the 7–3 compact scheme with 15 grid points is shown in Appendix A for a stretching grid with $\alpha = 0.8$. The variation of minimum required grid spacing $\Delta x_{\min}$ for stability with the high-order compact schemes is shown in Fig. 7. The figure shows that for up to 11th-order, the compact schemes can be stabilized by requiring $\Delta x_{\min}$ to be smaller than a certain number, however, the 12th-order compact scheme cannot be stabilized when the grids are stretched. The reason is currently not clear. Further studies are needed to understand the reason why compact schemes of very high order are not stable with high order boundary closure schemes. Hence, in this paper only moderately high order compact schemes (up to 11th-order) are presented. On the other hand, there is no stability problem for arbitrarily high-order explicit finite difference schemes, as long as the grid stretching is below the limits shown in Fig. 4.

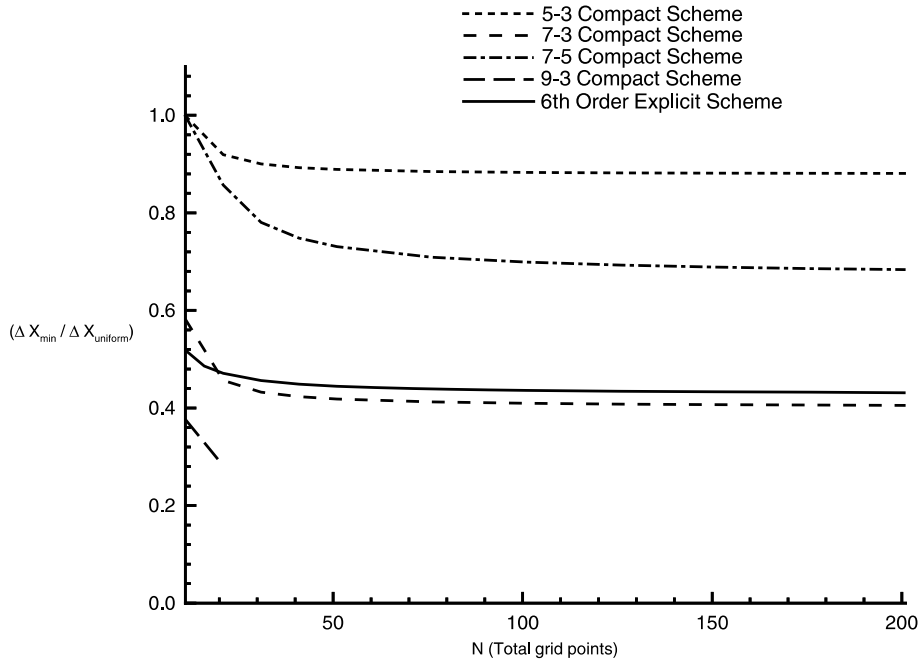

Fig. 7. Variation of minimum Δx required for stable boundary closure with the stencil width, for various compact schemes.

4.3. Stability of multi-dimensional high-order schemes

The stability analysis detailed in the previous subsection applies for a 1-D derivative operator only. The application to multidimensional problems requires the simultaneous application of high-order schemes to calculate spatial derivatives in several directions. The combined derivatives for 2-D and 3-D operators are much more complex than the 1-D case. In this section we show that the stability properties of the 1-D case are preserved for 2-D and 3-D cases if the matrix A has a complete set of eigenvectors. We address this issue by analyzing the scheme for a 2-D convective problem and choosing the following problem without loss of generality:

$$\frac{\partial u}{\partial t} = \frac{\partial u}{\partial x} + \frac{\partial u}{\partial y}, \tag{53}$$

where x, and y represent the coordinates of the two dimensions. The equation is discretized on a rectangular domain with N grid points in the x direction and M grid points in the y direction. The derivatives for a group of u's along a horizontal grid line in the x direction can be calculated as follows:

$$\frac{\partial}{\partial x}\begin{pmatrix} u_{1j} \\ u_{2j} \\ \vdots \\ u_{Nj} \end{pmatrix} = A_{N\times N}\begin{pmatrix} u_{1j} \\ u_{2j} \\ \vdots \\ u_{Nj} \end{pmatrix} \tag{54}$$

for $j = 1, 2, \ldots, M$ where A is the derivative matrix for the x direction. Similarly the y derivatives for a group of u's along a vertical grid line are as follows:

$$\frac{\partial}{\partial y}\begin{pmatrix} u_{i1} \\ u_{i2} \\ \vdots \\ u_{iM} \end{pmatrix} = B_{M\times M}\begin{pmatrix} u_{i1} \\ u_{i2} \\ \vdots \\ u_{iM} \end{pmatrix} \tag{55}$$

for $i = 1, 2, \ldots, N$ where B is the derivative matrix for the y direction. For a 1-D case considering A and B separately, we can determine the stability of the schemes by checking the eigenvalues α_i (for A) and β_j (for B), respectively. For a 2-D case the unknown variables are usually represented by a single vector of length $N \times M$. However, for the convenience of the following proof the the unknown variables located at all the grid points are represented by a matrix function as follows:

$$X = \begin{pmatrix} u_{11} & u_{12} & \ldots & & u_{1M} \\ u_{21} & \ddots & & & u_{2M} \\ \vdots & & u_{ij} & & \vdots \\ & & & \ddots & \\ u_{N1} & & & \ldots & u_{NM} \end{pmatrix}. \tag{56}$$

The spatial discretization of Eq. (53) leads to a system of ordinary differential equations

$$\frac{\partial X}{\partial t} = A \cdot X + X \cdot B^{\mathrm{T}}. \tag{57}$$

In Eq. (57) we can assume $X = \widetilde{X}e^{\lambda_k t}$ to get an eigenvalue problem for 2-D equations:

$$\lambda_k \widetilde{X}_{N\times M} = A_{N\times N}\widetilde{X} + \widetilde{X}B^{\mathrm{T}}_{M\times M}. \tag{58}$$

In this section we will prove the following theorem:

Theorem. *If A is diagonalizable and has eigenvalues α_i $(i = 1, 2, \ldots, N)$, and B is diagonalizable and has eigenvalues β_j $(j = 1, 2, \ldots, M)$, then the 2-D eigenvalue problem given by Eq.* (58) *will have eigenvalues λ_k $(k = 1, 2, \ldots, NM)$ as follows*:

$$\lambda_k = \alpha_i + \beta_j \begin{pmatrix} i = 1, \ldots, N, \\ j = 1, \ldots, M. \end{pmatrix} \tag{59}$$

Proof. The derivative matrix A can be written as:

$$A = P\Lambda_A P^{-1} (N \times N \text{ matrix}), \tag{60}$$

where

$$[\Lambda_A] = \begin{pmatrix} \alpha_1 & & \ldots & & 0 \\ & \ddots & & & \\ \vdots & & \alpha_i & & \vdots \\ & & & \ddots & \\ 0 & & & \ldots & \alpha_N \end{pmatrix} \tag{61}$$

and similarly B can be written as:

$$B = Q\Lambda_B Q^{-1} (M \times M \text{ matrix}). \tag{62}$$

Using the unknown variable matrix (Eq. (56)) we can write:

$$\frac{\partial X}{\partial x} = [AU_1 AU_2 \cdots AU_M] = AX, \tag{63}$$

where

$$U_j = \begin{pmatrix} u_{1j} \\ u_{2j} \\ \vdots \\ u_{Nj} \end{pmatrix}. \tag{64}$$

Similarly

$$\frac{\partial X}{\partial y} = \begin{pmatrix} V_1 B^{\mathrm{T}} \\ V_2 B^{\mathrm{T}} \\ \vdots \\ V_N B^{\mathrm{T}} \end{pmatrix}. \tag{65}$$

The analysis for the proof is as follows:

$$A = P\Lambda_A P^{-1}. \tag{66}$$

Hence, the eigenvalue problem can be written for each scalar eigenvalue λ_k as:

$$\lambda_k P^{-1}\widetilde{X} = \Lambda_A P^{-1}\widetilde{X} + P^{-1}\widetilde{X}B^{\mathrm{T}}. \tag{67}$$

Define

$$\widetilde{Y} = P^{-1}\widetilde{X} = \begin{pmatrix} l_1^A \widetilde{X} \\ l_2^A \widetilde{X} \\ \vdots \\ l_N^A \widetilde{X} \end{pmatrix} = \begin{pmatrix} y_1 \\ y_2 \\ \vdots \\ y_N \end{pmatrix}. \tag{68}$$

Hence, the eigenvalue problem for each scalar eigenvalue λ_k can be rewritten as follows:

$$\lambda_k \widetilde{Y} = \Lambda_A \widetilde{Y} + \widetilde{Y}B^{\mathrm{T}}, \tag{69}$$

$$(\lambda_k I - \Lambda_A)\widetilde{Y} = \widetilde{Y}B^{\mathrm{T}}, \tag{70}$$

$$\begin{pmatrix} \lambda_k - \alpha_1 & & \cdots & & 0 \\ & \ddots & & & \\ \vdots & & \lambda_k - \alpha_i & & \vdots \\ & & & \ddots & \\ 0 & & & \cdots & \lambda_k - \alpha_N \end{pmatrix} \begin{pmatrix} y_1 \\ \vdots \\ y_N \end{pmatrix} = \begin{pmatrix} y_1 \\ \vdots \\ y_N \end{pmatrix} B^{\mathrm{T}}, \tag{71}$$

$$\begin{pmatrix} (\lambda_k - \alpha_1)y_1 \\ \vdots \\ (\lambda_k - \alpha_N)y_N \end{pmatrix} = \begin{pmatrix} y_1 B^{\mathrm{T}} \\ \vdots \\ y_N B^{\mathrm{T}} \end{pmatrix}, \tag{72}$$

$$(\lambda_k - \alpha_i)y_i = y_i \cdot B^{\mathrm{T}} \quad (i = 1, \ldots, N), \tag{73}$$

$$(\lambda_k - \alpha_i)y_i^{\mathrm{T}} = B y_i^{\mathrm{T}}. \tag{74}$$

Hence, $(\lambda_k - \alpha_i)$ is an eigenvalue of B, giving:

$$\lambda_k = \alpha_i + \beta_j \begin{pmatrix} i = 1, \ldots, N, \\ j = 1, \ldots, M. \end{pmatrix} \tag{75}$$

Hence, if the one-dimensional schemes (associated with the matrices A and B) are stable then from the above relation we can conclude that the 2-D schemes are also stable. This analysis can easily be extended to the 3-D case and is not presented here.

In the above subsections we have shown that by using an appropriate stretching of the grids, with grids clustered near the boundaries, it is possible to derive asymptotically stable schemes on non-uniform grids. We have also presented methods to explicitly derive the coefficients for the numerical schemes. In addition, we have proved that the asymptotic stability properties of the 1-D case are preserved for the 2-D and 3-D cases if the derivative matrices have complete sets of eigenvectors. In the following section, the high-order non-uniform grid schemes are numerically tested by considering a one-dimensional wave equation problem and 2-D incompressible flow simulations.

5. Numerical results

The high order explicit and compact schemes are first tested by solving the one-dimensional linear wave equation. The purpose of this test is to confirm the numerical stability of the high-order schemes and to quantitatively evaluate the accuracy of the high-order schemes. It is shown that high-order schemes (tested up to 17th-order) offer very good accuracy, which is important for flow simulations with a wide range of length scales, such as the direct numerical simulation of transitional and turbulent flows.

The new non-uniform grid high-order schemes are derived based on analysis on linear model equations only. Hence, the new scheme is applied to 2-D incompressible flow problems to determine whether the good performance and stability of the high-order schemes shown in the model equations can be maintained when the high-order schemes are applied to nonlinear Navier–Stokes equations. The results from the test cases are presented in the following subsections. Once, the schemes were tested, they were applied to the direct numerical simulations of 3-D compressible full Navier–Stokes equations. For simplicity, only the explicit schemes were used for the Navier–Stokes computations. However, we expect the stability of high-order stretched grid compact schemes to hold for such computations as well.

5.1. Wave equation computations

The model equation used for the one-dimensional wave equation computations is given by Eq. (50). The non-periodic boundary condition is set at the left boundary as

$$u(-1, t) = \sin(\omega \pi t) \quad t \geqslant 0. \tag{76}$$

The wave equation is solved in a fixed computational domain $(-1, 1)$. The parameters of the calculations are: $c = 1$, $\omega = 1$. The computations are performed using the second-, fourth-, sixth-, eighth-, 10th-, and 12th-order explicit schemes. All the computations are performed on the same stretched grid with the stretching parameter $\alpha = 0.91$, which leads to a stable scheme for all the above orders of accuracy. The boundary closure scheme used is of the same order as the interior so that there is no loss of accuracy due to the boundary schemes. The value of the the grid stretching parameter, $\alpha = 0.91$, is chosen such that the stability condition for all the above high order schemes is satisfied. The calculations are done using 21, 41, 51, and 101 grids. The time stepping scheme used in the computations is a fourth-order Runge–Kutta scheme. The time step is chosen and tested to be small enough such that the temporal errors are always smaller than spatial errors in order to test the numerical accuracy of the spatial high-order schemes.

As expected, the computations of all orders are numerically stable with even high-order boundary closure schemes. Fig. 8 shows a typical result on the comparison for 16th-order scheme on a stretched grid with the stretching parameter $\alpha = 0.91$. The boundary closure is now stable and there is excellent agreement between the numerical and exact solutions. The error distribution for the 10th-order scheme is shown in Fig. 9. The average error for all the schemes and grid sizes are shown in Fig. 10. The results show the advantage of using higher order schemes. The errors of the results using 21 grid points reduced substantially when the order of the schemes increases. The error of a second-order scheme is 3×10^{-2} using 21 points. The error reduced to 6×10^{-10} for the 12th-order scheme. The stretching allows high order accuracy and stability to be maintained at the boundary. The resolution of numerical scheme was further tested using a case with multiple frequencies. This is done by modifying the boundary condition as follows:

$$u(-1, t) = \sum_{i=1}^{N} \sin(\omega_i \pi t + \phi_i) \quad t \geqslant 0, \tag{77}$$

where the phase of each mode ϕ_i was chosen randomly. Fig. 11 shows the excellent agreement of the numerical solution, computed using a 12th-order scheme, with the exact solution.

The resolution ability of the schemes is further studied by computing the dispersive errors using a Fourier analysis when they are applied to Eq. (50). The trial solution is

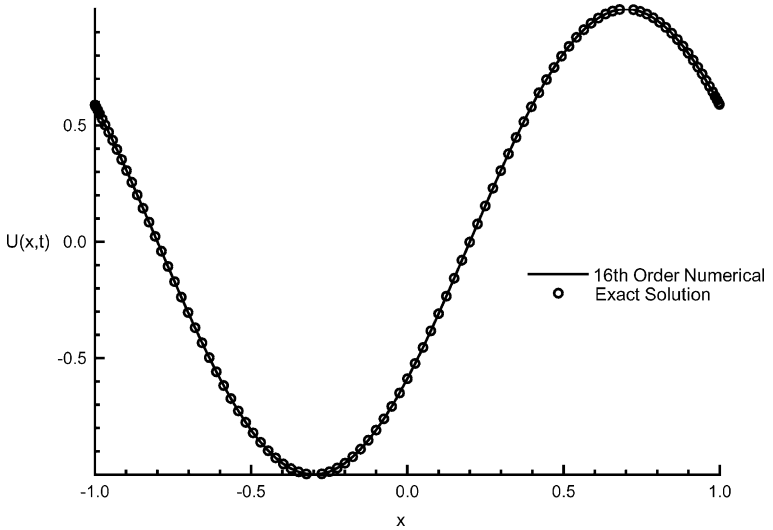

Fig. 8. Comparison of numerical solution, using a 16th-order explicit scheme on a stretched grid ($\alpha = 0.91$), with the exact solution at $t = 2.2$ s.

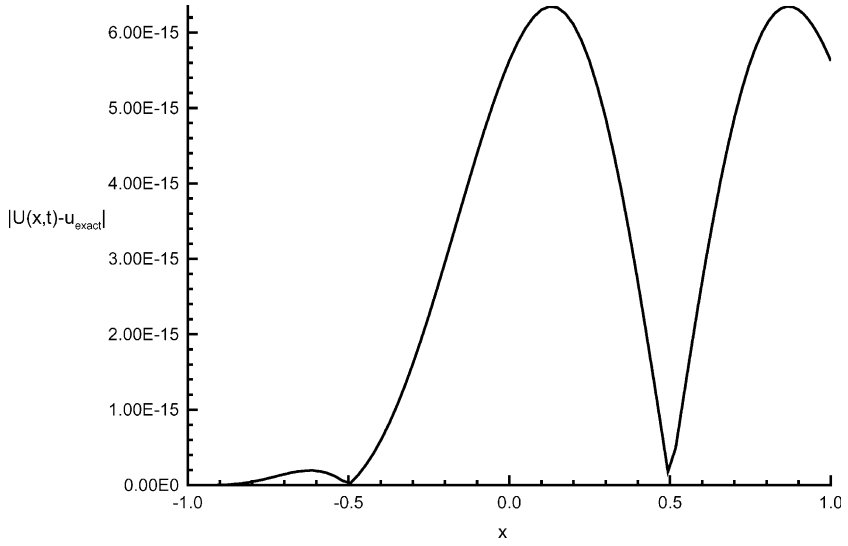

Fig. 9. Error distribution for numerical solution, using a 10th-order explicit scheme on a stretched grid ($\alpha = 0.91$), at $t = 1$ s.

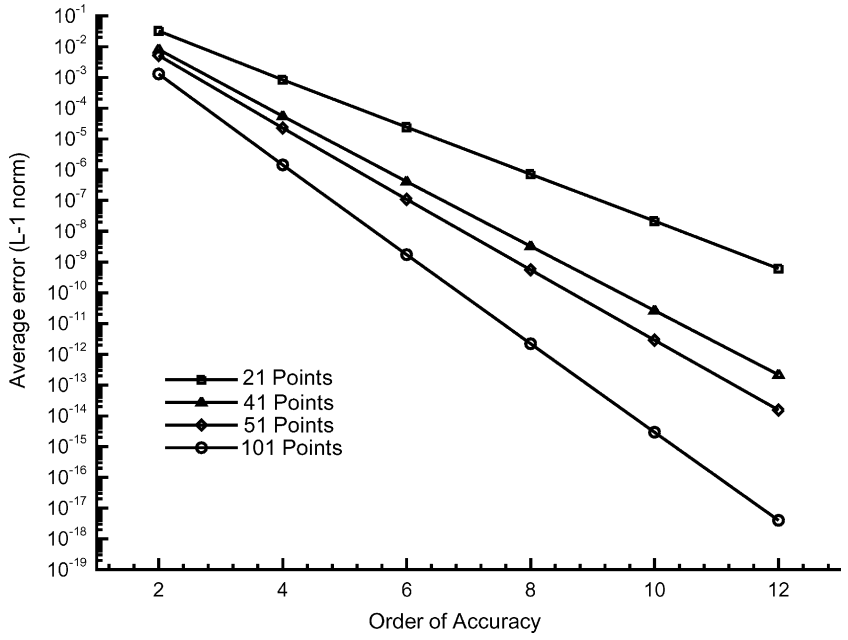

Fig. 10. Average error (L-1 norm) for explicit high order scheme solutions of the wave equation.

$$u = u(t)\mathrm{e}^{\mathrm{i}\omega x/h}, \tag{78}$$

where h is the largest grid spacing for the particular grid chosen. The exact derivative of the trial solution is

$$\frac{\partial u}{\partial x} = \frac{\mathrm{i}\omega}{h}u. \tag{79}$$

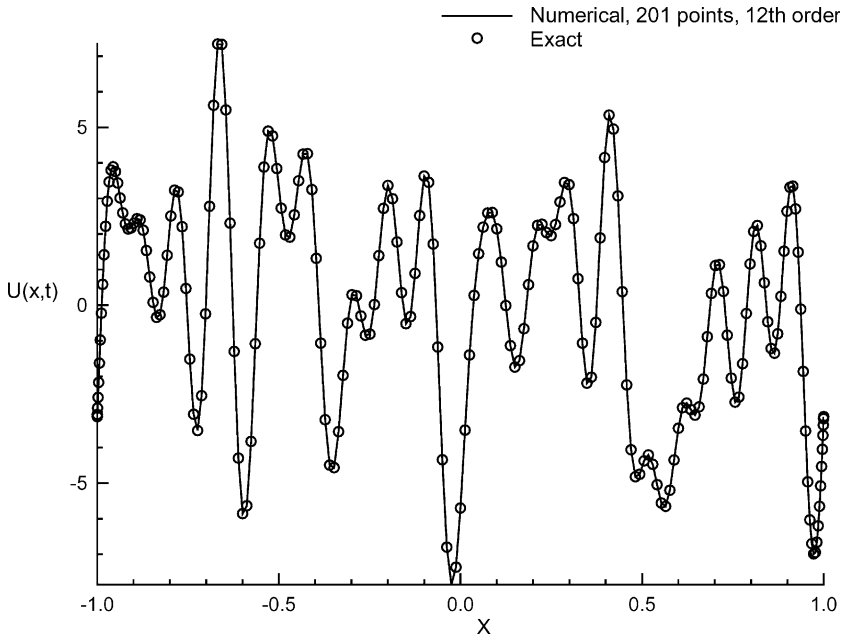

Fig. 11. Comparison of numerical solution, computed using a 12th-order scheme, and the exact solution for the multiple wavenumber and random phase test case for the wave equation.

Applying the trial function to a finite difference scheme given by Eq. (30) leads to

$$\frac{\partial u}{\partial x} = \frac{\mathrm{i}\omega_1}{h} u, \tag{80}$$

where

$$\omega_1 = -i \sum_{k=1}^{n} b_{i,k}\, \mathrm{e}^{\mathrm{i}(x(k)-x(i))\omega/h}. \tag{81}$$

The dimensionless dispersive errors are calculated as follows:

$$\text{Dispersive Errors} = Re(\omega_1 - \omega). \tag{82}$$

It should be noted that the dispersive errors will be different at various points of the grid (unlike the uniform grid case). In this paper we present the maximum dispersion errors. The dispersion plot of ω_1 vs ω for the first derivative is shown in Fig. 12. The figure shows that as the stencil width is increased the resolution of the scheme improves and the dispersion errors are reduced. Hence, by choosing a higher order scheme, made possible because of the stability of the high order boundary closure on non-uniform grids, we can resolve a large range of scales. The dissipation errors can be calculated in a similar manner. However, the dissipation errors are a few orders of magnitudes smaller than the dispersive errors and are not presented here.

On the other hand, the computations using sixth-order or higher schemes are not stable if the grid is uniform. Fig. 13 shows a typical result of the comparison of the numerical solution with the exact solution for a sixth-order interior and boundary scheme on a uniform grid at $t = 2.2$ s. The instability at the boundary can be seen. This instability will develop rapidly and lead to a diverged numerical solution at later time steps. Another test case considered solutions on a stretched grid and used a high-order scheme derived

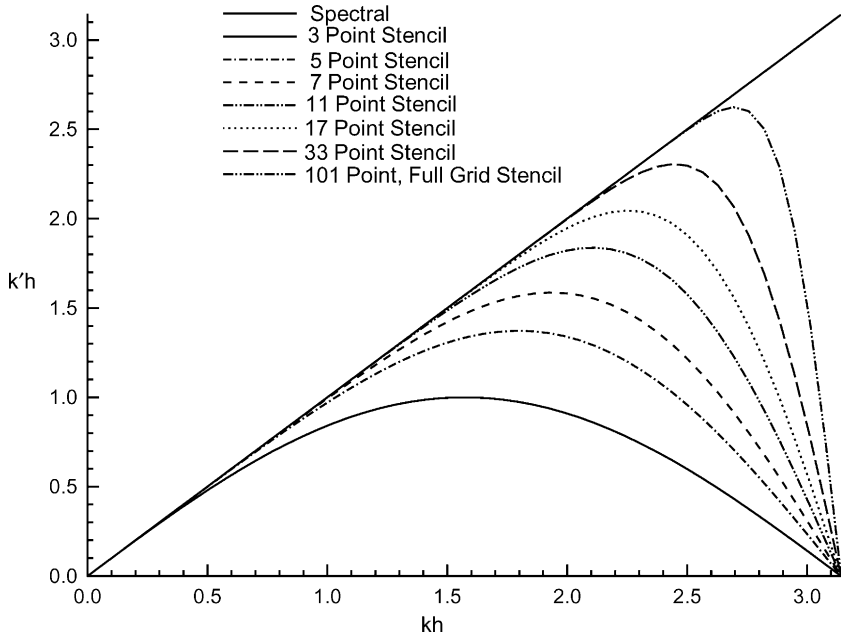

Fig. 12. Comparison of modified wavenumber for the first derivative, for various non-uniform grid schemes.

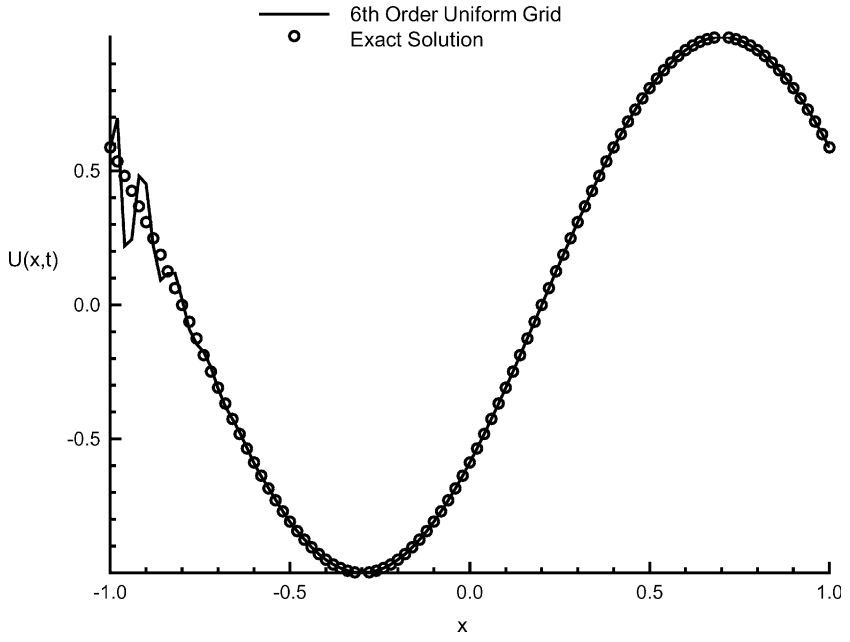

Fig. 13. Comparison of numerical solution , using a sixth-order explicit scheme on an uniform grid, with the exact solution at $t = 2.2$ s.

on a uniform computational coordinates through a coordinate transformation This case also leads to numerical instability at the boundary and is unstable. Fig. 14 shows the comparison of numerical solution (at $t = 0.01$ s) using the stretched grid computed by a sixth-order explicit scheme on a uniform grid through

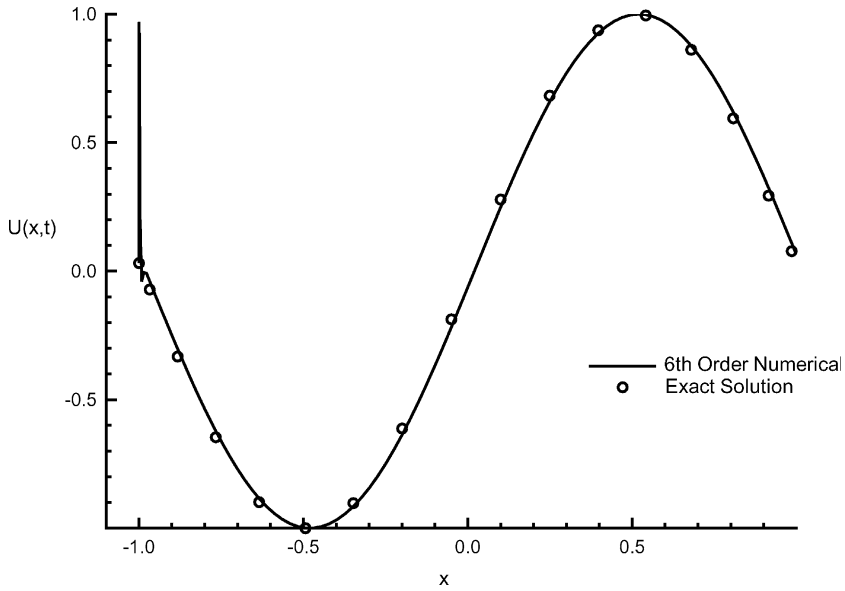

Fig. 14. Comparison of numerical solution (at $t = 0.01$ s) using a stretched grid and is computed by a sixth-order explicit scheme on a uniform grid through coordinate transformation.

coordinate transformation. The computations develop numerical instability at the boundary and will diverge at a later time. Hence, using a high order numerical scheme derived on a uniform grid, with or without a grid transformation, leads to an unstable solution. However, as demonstrated earlier, the application of the scheme directly on an appropriately stretched grid leads to stable solution even with high order boundary closure schemes.

5.2. Two dimensional incompressible viscous flows

The results from the previous subsection show that the new non-uniform grid high order schemes are stable with high order boundary closure for linear wave equations. However, the Navier–Stokes equations have nonlinear terms which may lead to instability when discretized by the new schemes. Hence, in this subsection we use the scheme to solve incompressible Navier–Stokes equations, and evaluate if the new scheme continues to be stable and accurate for nonlinear problems. A simple flat plate geometry is used in the simulations. Steady Blasius boundary layer test cases are considered to evaluate the stability and resolution of the new schemes.

5.2.1. Governing equations

The governing equations are the incompressible Navier–Stokes equations in the vorticity transport form [31] which is a standard form used in direct numerical simulations of incompressible flows:

$$\frac{\partial \omega_z}{\partial t} + \frac{\partial}{\partial x}(u\omega_z) + \frac{\partial}{\partial y}(v\omega_z) = \Delta\omega_z, \tag{83}$$

where the Δ operator is defined as:

$$\Delta = \frac{1}{Re}\frac{\partial^2}{\partial x^2} + \frac{\partial^2}{\partial y^2}. \tag{84}$$

The flow variables are nondimensionalized as follows:

$$x = \frac{x^*}{L}, \quad y = \sqrt{Re}\frac{y^*}{L}, \quad z = \frac{z^*}{L}, \quad u = \frac{u^*}{U_\infty}, \quad v = \sqrt{Re}\frac{v^*}{U_\infty}, \tag{85}$$

where the $*$'s represent the dimensional variables and $Re = U_\infty L/v$. The velocity components can be calculated from the following equations:

$$\Delta v = -\frac{\partial \omega_z}{\partial x}, \tag{86}$$

$$\frac{\partial^2 u}{\partial x^2} = -\frac{\partial^2 v}{\partial x \partial y}. \tag{87}$$

The Blasius boundary layer solution is prescribed at the inlet. No slip conditions are used on the wall. The vorticity at the wall is computed from the following equation:

$$\frac{\partial \omega_z}{\partial x} = -\Delta v. \tag{88}$$

At the free stream ω_z is set to zero. The streamwise velocity is fixed and the wall normal velocity is computed from the continuity equation. The exit flow properties are calculated using the governing equations and setting the $(1/Re)(\partial^2/\partial x^2)$ terms to zero.

5.2.2. Non-uniform grid high-order finite difference method

The equations are discretized on a stretched grid in both directions using Eq. (26), with the derivative coefficients computed directly for the non-uniform grid. In this test case the physical domain is rectangular and no transformations are required to solve the equations. The convective terms are discretized using a high order upwind finite difference scheme. The upwinding is done using a biased stencil (shifted by one point) with the same order as the overall scheme. The order can be set to an arbitrarily high number less than the number of grid points. The second derivatives in the viscous terms are discretized directly on the stretched grid using high order finite differences. In addition, the formulas for normal velocity derivatives on the wall include the first derivative at the wall (i.e., a compact scheme is used at the wall) to ensure that the continuity equation is satisfied. The solution is advanced in time using a fourth-order Runge–Kutta method.

5.2.3. Flat plate boundary layer test case

The high order incompressible explicit Navier–Stokes code was tested by computing a flat plate boundary layer test case. The numerical solution is compared with the self-similar Blasius boundary layer solution. The flow variables are nondimensionalized as follows:

$$x = \frac{x^*}{L}, \quad y = \sqrt{Re}\frac{y^*}{L}, \quad z = \frac{z^*}{L},$$

$$u = \frac{u^*}{U_\infty}, \quad v = \sqrt{Re}\frac{v^*}{U_\infty}, \quad w = \frac{w^*}{U_\infty}. \tag{89}$$

In this test case the Reynolds number is 10^5 and the characteristic length is 0.05 m. The domain ranges $x_0 = 0.37$ to $x_N = 0.5$ in the x-direction and the maximum in the wall normal direction is $y_N = 18.84$. A 101×101 grid, with the grid stretching parameter $\alpha = 0.98$, is used for the calculations. The computations are carried out using third, seventh, ninth, and 15th-order schemes. Fig. 15 shows the variation of the wall

normal velocity in the wall normal direction at $x = 0.469$ for the 15th-order case, and compares it to the exact solution obtained from the Blasius boundary layer equations. The solution is in very good agreement with the Blasius solution. The vorticity contours for the 15th-order case are shown in Fig. 16. The contours show that the solution is smooth and stable for a 15th-order scheme with 15th-order boundary closure. Such a scheme is unstable on a uniform grid and will show large oscillations in the contours. The relative errors for the schemes of various order are shown in Fig. 17. While calculating the errors, the solution using

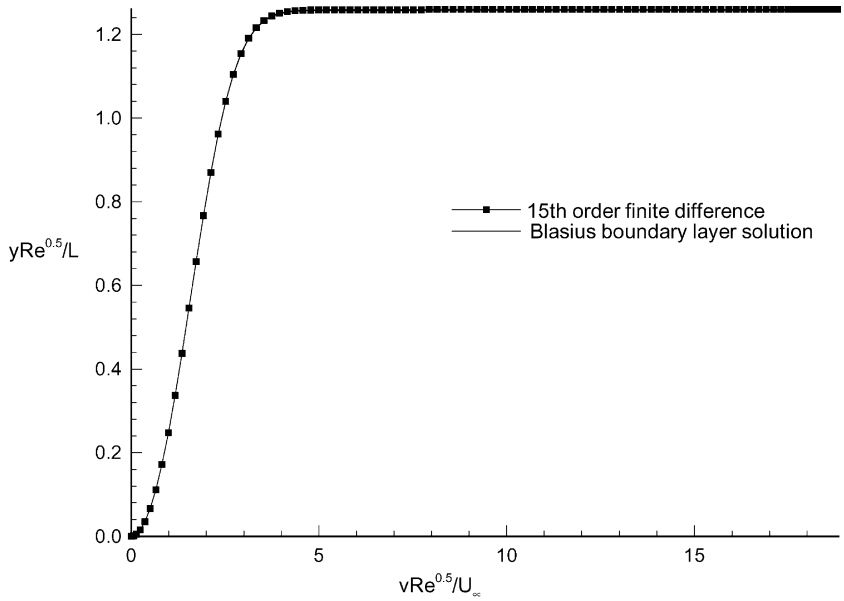

Fig. 15. Comparison of the wall normal velocity numerical solution with the Blasius solution, at $x/L = 0.469$. The numerical solution is calculated using the 15th-order scheme.

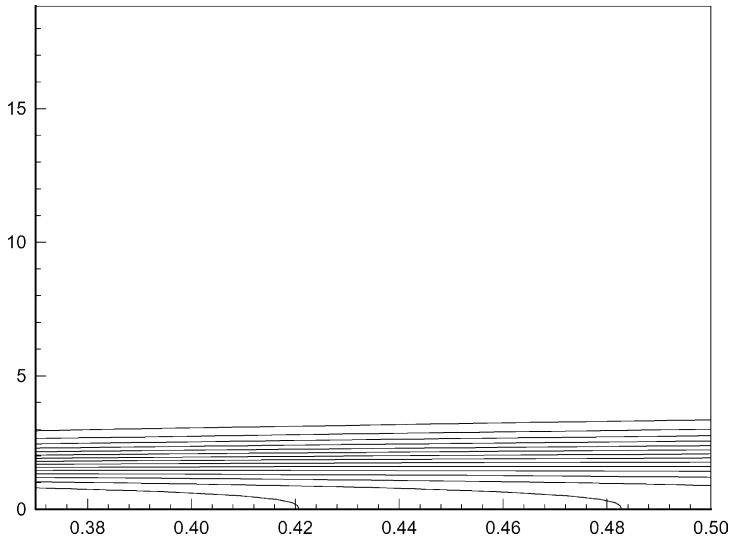

Fig. 16. Spanwise vorticity contours for the incompressible flat plate boundary layer case. The numerical solution is calculated using the 15th-order scheme.

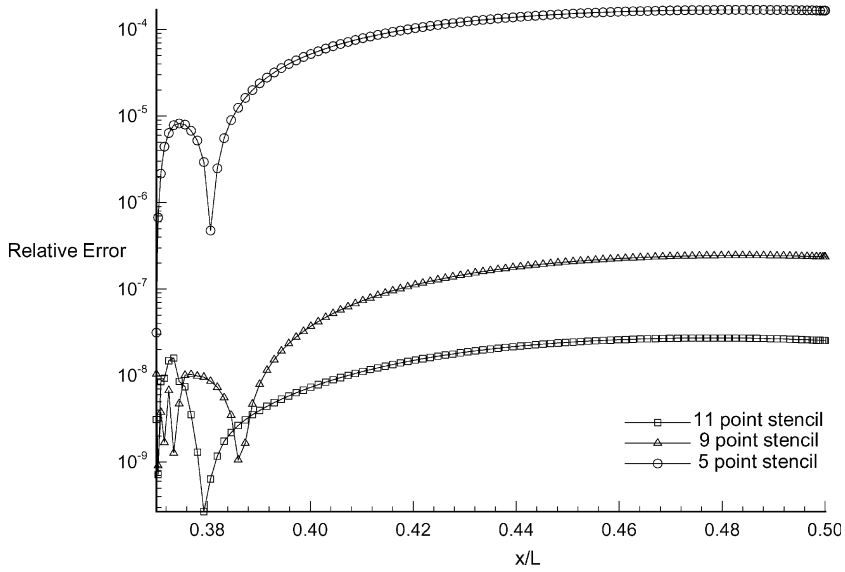

Fig. 17. Comparison of the wall vorticity distribution errors computed using the third, seventh, and ninth-order schemes.

the 15th-order scheme is chosen as the exact solution. As expected, the accuracy of the solution improves as the order of the schemes is increased from third to 15th-order.

As shown in the above subsections the new non-uniform grid schemes are stable and accurate for simulations of the wave equation, and the incompressible Navier–Stokes equations. The solutions obtained are in excellent agreement with the exact solutions in both cases. Hence, the new schemes are applicable to both linear and nonlinear problems, with arbitrarily high orders of accuracy with high order boundary closure schemes. In the next section, the schemes are applied for the direct numerical simulation of the receptivity processes in hypersonic boundary layer transition.

6. Receptivity of Mach 15 flow over a parabola

In this section, we apply the new high-order non-uniform grid schemes to compute the receptivity process of hypersonic boundary layer flows over a parabolic blunt leading edge. The receptivity mechanism provides important initial conditions of amplitude, frequency, and phase of instability waves in the boundary layers. The same test case was considered by Zhong [32] using a fifth-order shock fitting scheme. The receptivity problem is an ideal case to test the new schemes because it involves both steady and unsteady flow simulation in a viscous hypersonic flow field. The unsteady flow field contains complex interaction of a number of waves of different length scales. It is expected that high-order schemes will be particularly useful in capturing the different length scales effectively.

Specifically, the receptivity of a two-dimensional boundary layer to free stream acoustic waves for hypersonic flows past a parabolic leading edge at zero angle of attack are considered. The parabolic body surface is determined by:

$$x^* = b^* y^{*2} - d^*, \tag{90}$$

where b^* and d^* are constants, and d^* is used as the reference length in this paper. The nose radius of curvature is $r^* = 1/(2b^*)$. Free stream disturbances are superimposed on a steady mean flow before reaching the bow

shock to investigate the process of free stream waves entering the boundary layer and inducing boundary-layer waves. The free stream disturbances are assumed to be weak monochromatic planar acoustic waves with wave fronts normal to the center line of the body. The wave fields are represented by the perturbations of instantaneous flow variables with respect to their local steady based flow variables at the same location. The flow is characterized by a free stream Mach number $M_\infty = u^*_\infty/a^*_\infty$, and a Reynolds number defined by

$$Re_\infty = \frac{\rho^*_\infty U^*_\infty d^*}{\mu^*_\infty}. \tag{91}$$

The forcing frequency of the free stream acoustic wave is represented a dimensionless frequency F defined by

$$F = 10^6 \ \frac{\omega^* v^*}{U^{*2}_\infty} = 10^6 \ \omega/Re_\infty, \tag{92}$$

where F represents the wave frequency with respect to viscous flow scales. We can also define a Strouhal number S uisng the nose radius by

$$S = \frac{\omega^* r^*}{U^*_\infty}, \tag{93}$$

where r^* is the nose radius. The Strouhal number represents the relative nose bluntness in the receptivity problem.

The flow conditions of the current computational case are as follows. $M_\infty = 15$, $T^*_\infty = 192.989$ K, $p^*_\infty = 10.3$ Pa, $\gamma = 1.4$, $Pr = 0.72$, $R^* = 286.94$ Nm/kg K, $Re_\infty = 6026.6$, $T^*_w = 1000$ K, $r^* = 0.0125$ m, $d^* = 0.1$ m, and $\epsilon = 5 \times 10^{-4}$–$10^{-1}$. The nondimensional frequency is $k_\infty = 15$, and $F = 2655$, $S = 2$. Two sets of grids are used to compute both steady and unsteady flow solutions of the full Navier–Stokes equations: a coarse 31×51 grid and a finer 51×91 grid. The computational grid of 31×51 is shown in Fig. 2. For each grid, the flow solutions are simulated using a non-uniform grid scheme of different orders. Specifically, the orders are first-, third-, fifth-, seventh-, ninth-, and 11th-order. The grid stretching parameter α in Eq. (26) is 0.6, which has been found to be stable for the various order schemes computed.

Because the flow field behind the bow shock is not uniform, the flow variables are nondimensionalized using the free stream conditions as characteristic variables. Specifically, we nondimensionalize the velocities with respect to the free stream velocity U^*_∞, length scales with respect to a reference length d^*, density with respect to ρ^*_∞, pressure with respect to p^*_∞, temperature with respect to T^*_∞, time with respect to d^*/U^*_∞, vorticity with respect to U^*_∞/d^*, entropy with respect to c^*_p, wave number by $1/d^*$, etc. The dimensionless flow variables are denoted by the same dimensional notation but without the superscript "$*$".

6.1. Steady base flow solutions

The steady base flow solutions of the Navier–Stokes equations for the Mach 15 flow over the blunt leading edge are obtained first by advancing the solutions to a steady state without free stream perturbations. The physical characteristics of the solutions of this flow problem have been discussed in detail in [19]. The main focus of this paper is to evaluate the numerical stability and accuracy of high-order non-uniform grid schemes at different orders and different grid resolutions.

Fig. 18 shows the Mach number contours and velocity vectors for steady base flow solutions using the 11th-order non-uniform grid scheme. The results computed by the 11th-order scheme are very smooth for this relatively coarse grid. Non-uniform grid schemes of the first-, third-, fifth-, ninth-, and 11th-order were used to solve the base flow using the same 31×51 grid to evaluate the numerical accuracy. Since there is no analytical solution available, we evaluate the numerical accuracy by comparing the present solutions with those of an 11th-order scheme using a finer 51×91 grid. Fig. 19 shows such accuracy evaluation for the

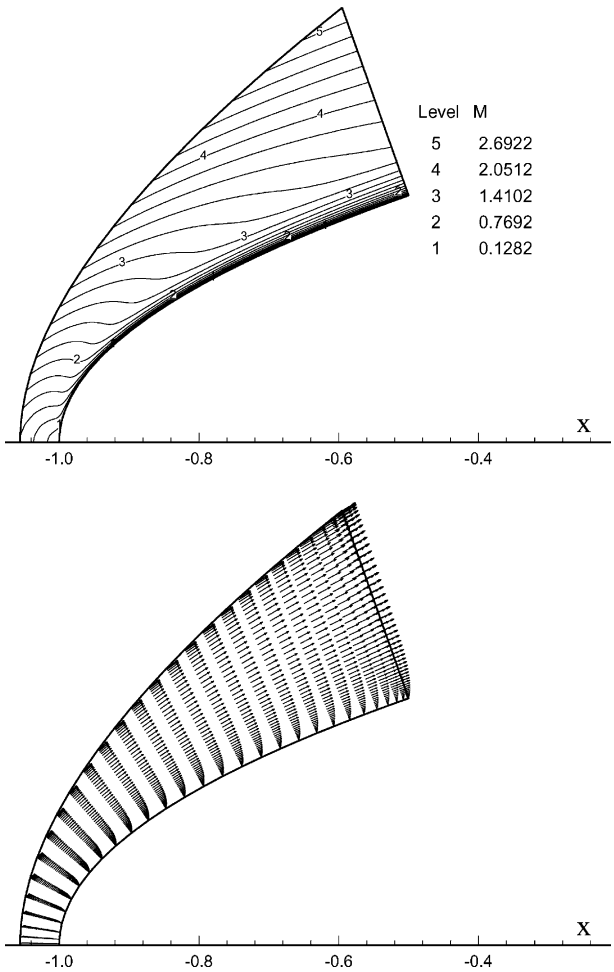

Fig. 18. Mach number contours and velocity vectors for steady base flow solutions using the 11th-order non-uniform grid scheme (31×51 grid).

surface distribution of vorticity using non-uniform grid schemes of different orders. The lower figure shows the comparison near the minimum vorticity point. Again the figure shows the improvement of numerical accuracy as the order of the method increases. The 11th-order scheme using the coarse grid is very close to the results of fine grid of the same order. Similar trends in the numerical accuracy of the results are also shown in the surface heating rates distribution (Fig. 20).

Fig. 21 show a quantitative assessment of the numerical accuracy of the schemes of different orders by plotting the relative errors of heating rates at the stagnation point. For a fixed grid resolution, the numerical accuracy of the schemes improves as the order of the schemes increases. The improvement is dramatic when the order is low. As the order increases, the improvement in accuracy becomes smaller. At very high-order, there is very little improvement in accuracy by increasing the order further, because it has reached the limit of the grid resolution. When a finer grid is used, the high-order schemes lead to further improvement of accuracy. Therefore, the accuracy of high-order schemes can be improved substantially by increasing the order of the schemes, but for a given grid resolution there is a limiting order of the schemes, beyond which the accuracy of the solutions can not be improved further unless the grid is further refined.

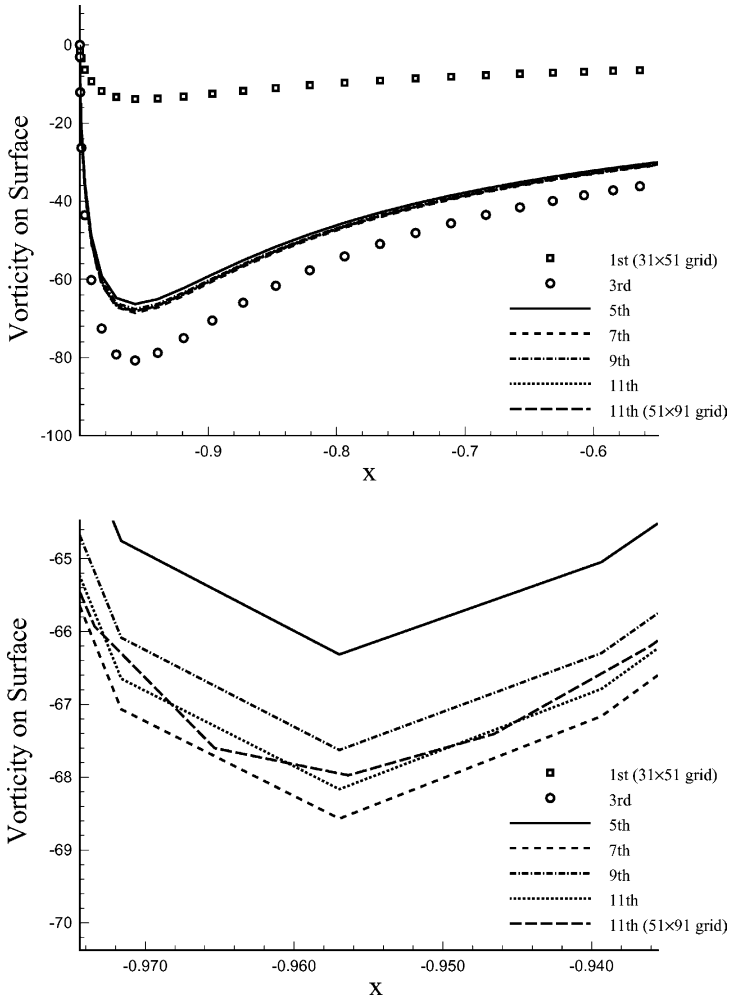

Fig. 19. Flow vorticity distribution along parabola surface for steady base flow solutions using non-uniform grid schemes of the following orders: first, third, fifth, ninth, 11th-order schemes using 31×51 grid and a case of 11th-order using a finer grid of 51×91. Lower figure shows the comparison near the minimum vorticity point.

For the current 2-D Navier–Stokes equations over a blunt body, the limiting order for the 31×51 grid is about fifth-order, while the limit for the finer 51×91 grid is ninth-order.

Overall, the steady-flow results show that the high-order non-uniform grid schemes are stable for very high-order (tested up to 11th-order) schemes. Such high order solutions are not possible using a conventional uniform grid scheme because of numerical instability. The high-order non-uniform grid schemes can produce highly accurate numerical solutions.

6.2. Unsteady flow solutions

Having obtained the steady solution, the receptivity of the hypersonic boundary-layer in the Mach 15 flow over the parabola is studied by numerical simulation using the high-order schemes. The high-order non-uniform grid schemes are used to compute the unsteady solutions induced by free stream acoustic

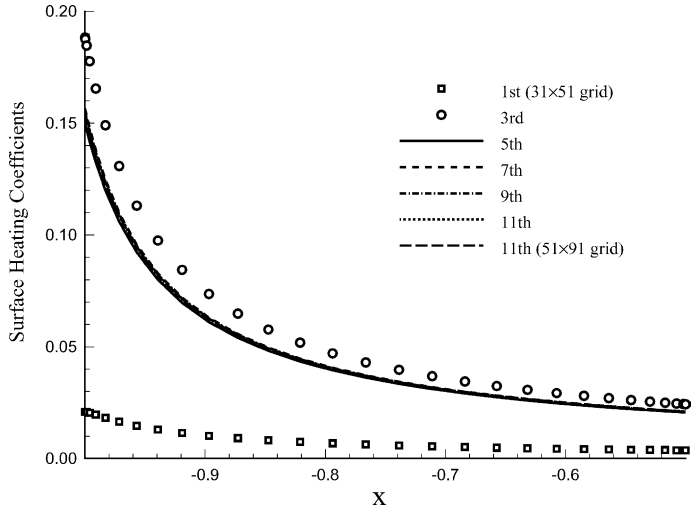

Fig. 20. Nondimensional heating rates distributions along parabola surface for steady base flow solutions using non-uniform grid schemes of different orders and different grids.

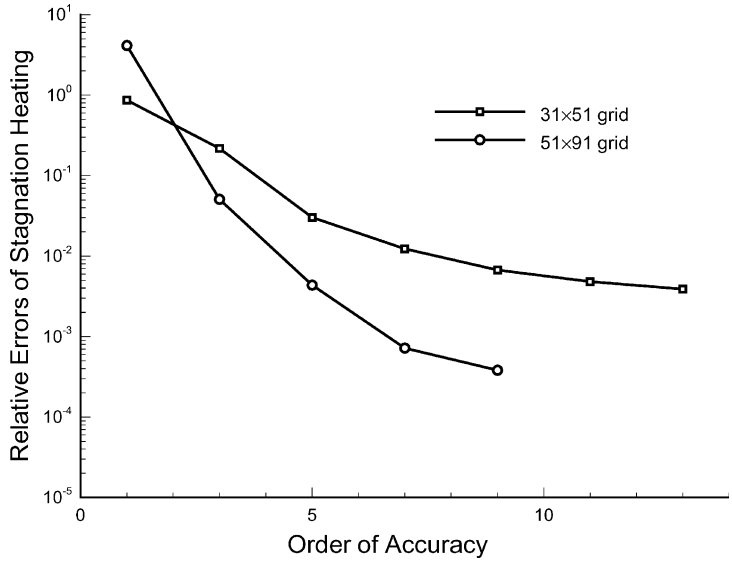

Fig. 21. Relative heating rate errors at the stagnation point for steady base flow solutions using non-uniform grid schemes of different orders and different grids.

waves. For weak disturbance waves in the free stream before reaching the bow shock, the perturbation of an arbitrary flow variable can be written in the following form:

$$q_\infty(x,y,t)' = |q'_\infty| e^{ik_\infty(x-c_\infty t)}, \tag{94}$$

where $q_\infty(x,y,t)$ represents the perturbation of any flow variables, $|q'_\infty|$ is the wave amplitude constant, k_∞ is the wave number, and c_∞ is the wave speed in the free stream before reaching the shock. For fast acoustic

waves the perturbation amplitudes of the nondimensional flow variables satisfy the following dispersion relations:

$$\underline{\text{Fast Acoustic Waves}(c^*_\infty = u^*_\infty + a^*_\infty)}: |\rho'|_\infty = |p'|_\infty/\gamma = |u'|_\infty M_\infty = \epsilon M_\infty, \quad |s'|_\infty = |v'|_\infty = 0,$$

where ϵ is a small number, and ϵM_∞ represents the relative amplitude of a free stream wave. The free stream wave number k_∞ is related to the circular frequency ω by $\omega = k_\infty c_\infty$. The forcing frequency of the free stream acoustic wave is represented by a dimensionless frequency F defined by

$$F = 10^6 \frac{\omega^* \nu^*}{U^{*2}_\infty} = 10^6 \omega / Re_\infty, \tag{95}$$

where F represents the wave frequency with respect to a viscous flow scale.

The forcing waves induce boundary layer waves inside the boundary layers. The unsteady calculations are carried out until the solutions reach a periodic state in time. Temporal Fourier analysis is carried out on

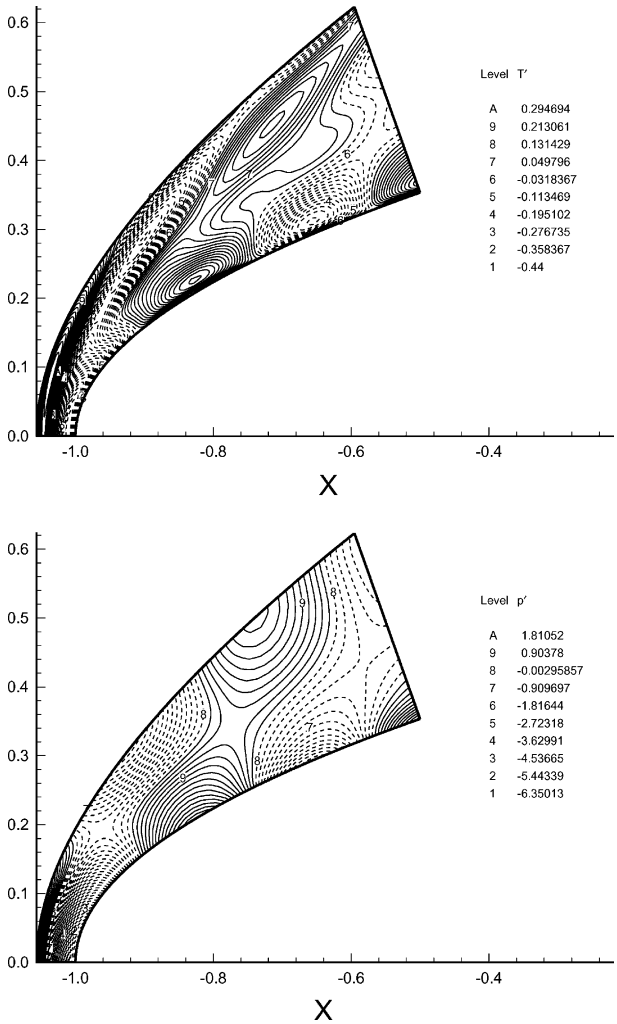

Fig. 22. Instantaneous temperature and pressure perturbation contours for the case of free stream acoustic wave of $F = 2655$ and wave amplitude of 0.001. The solution is obtained by the ninth-order schemes using 51×91 grid.

local perturbations of unsteady flow variables after a time periodic state has been reached. The Fourier transform for the real disturbance functions lead to:

$$q'(x,y,t) = \Re\left\{ \sum_{n=0}^{N} |q_n(x,y)| e^{i[-n\omega_0 t + \phi_n(x,y)]} \right\}, \tag{96}$$

where $n\omega_0$ is the frequency of the nth wave mode, $q'(x,y,t)$ represents any perturbation variables. The boundary layer waves contain the fundamental wave mode, which has the same frequency F as the forcing acoustic waves. At the same time, due to the nonlinear interaction, the wave field also contains higher harmonics of the fundamental frequency, nF, where $n = 0$ represents mean distortion, $n = 1$ represents the fundamental mode, $n = 2$ represents the second harmonics of two times the fundamental frequency, etc. The higher harmonics have smaller wave lengths and orders of magnitude smaller amplitudes. For example, the wavelength of $n = 2$ mode is about half of that of the $n = 1$ fundamental mode.

The results presented here are those for the case of free stream frequency of $F = 2655$ and nondimensional free stream forcing wave amplitude of $\epsilon = 0.001$. The unsteady solutions are computed by the new

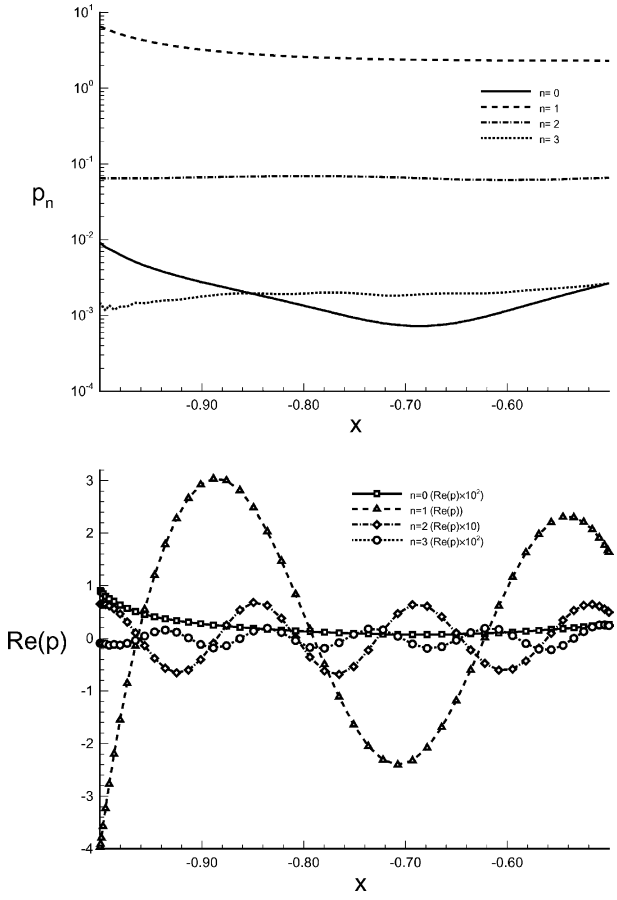

Fig. 23. Fourier amplitudes of pressure perturbation and their real part along parabola surface. The solution is obtained by the seventh-order schemes using 51×91 grid. In the figure, $n = 0, 1, 2, 3$, corresponds to mean flow distortion, fundamental mode, second harmonic, and third harmonic.

non-uniform grid schemes of different orders. Fig. 22 shows the instantaneous pressure and temperature perturbation contours. The solution is obtained by the ninth-order scheme using a 51×91 grid. The results show a very smooth wave solution. In response to the perturbations of the forcing waves in the free stream, the unsteady flow field produces boundary layer wave modes of fundamental frequencies and their harmonics. In the present case, the higher harmonics are several orders of magnitudes weaker than the fundamental modes. Fig. 23 shows the Fourier harmonics of the induced wave. It shows the Fourier amplitudes of pressure perturbation and their real parts along the parabola surface. The solution is obtained by the seventh-order schemes using a 51×91 grid. In the figure, $n = 0, 1, 2, 3$, corresponds to mean flow distortion, fundamental mode, second harmonic, and third harmonic. The figures show that the high-order schemes are able to capture these modes with a relatively coarse grid. Notice that there are about 27, 18, and 9 grid points per period for the first ($n = 1$), the second ($n = 2$), and third harmonic ($n = 3$), respectively. The amplitudes of these three harmonics are in the order of 10^1, 10^{-1}, and 10^{-3} for the first, second, and third harmonics. The figures show that the seventh-order scheme captures all these modes well.

The results of wave harmonics obtained by different order schemes of the same grid are compared in Figs. 24–26. The results shows that the fundamental mode is captured very well by the schemes of fifth, seventh, and ninth-order, but not well resolved by the third-order scheme. Fig. 25 shows that for the third harmonic ($n = 3$) the third-order scheme has significant errors compared to the fifth-, seventh-, and ninth-order schemes. All the schemes show insufficient resolution near the start of the domain. However, the fifth, seventh, and ninth-order schemes resolve the mode well in the interior of the domain, whereas the third-order scheme is not able to resolve the third harmonic. Similarly, the fifth-order scheme under predicts the mean flow distortion ($n = 0$ mode) caused by nonlinear wave interaction. Therefore, the ninth-order scheme produces more accurate results than the fifth-order scheme for the transient flow field when the length scale is small for the high harmonics and the mean flow distortion due to nonlinear interactions.

Similar to the steady solution case, it is necessary to have sufficient grid resolution for the flow length scale in order to have good accuracy. The corresponding unsteady flow have also been computed by using a

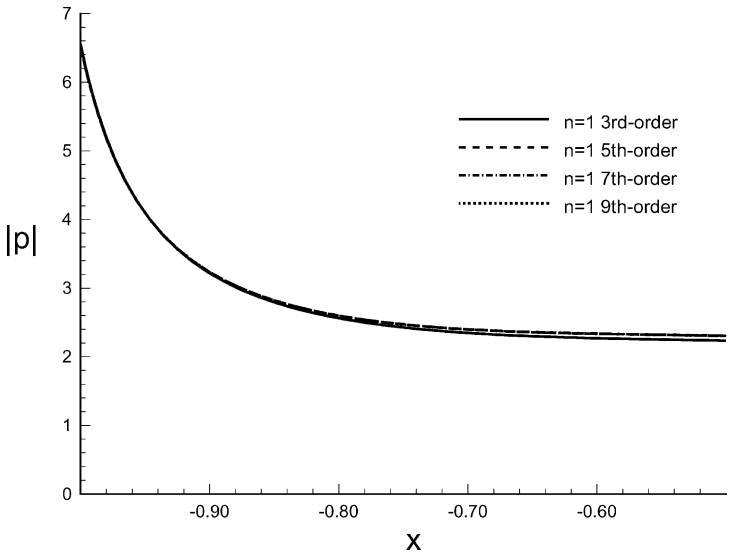

Fig. 24. Fundamental mode ($n = 1$) pressure perturbation amplitudes along parabola surface. The solution is obtained by the third, fifth, seventh, and ninth-order schemes using 51×91 grid.

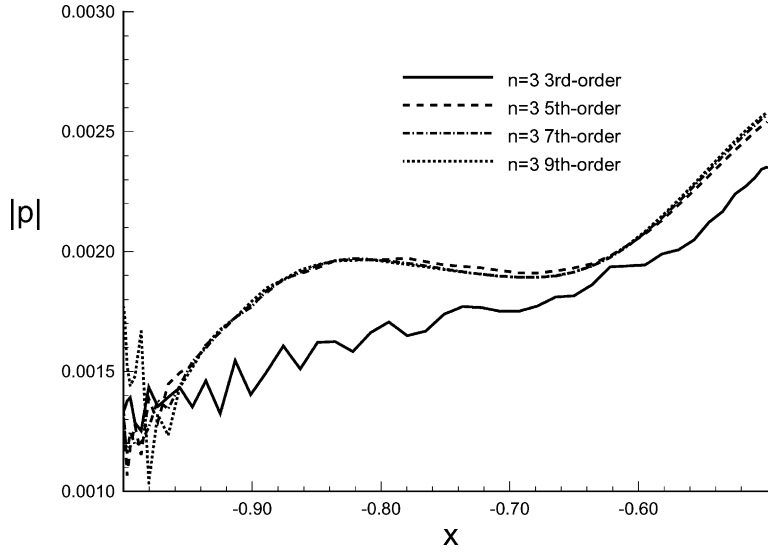

Fig. 25. Third harmonic ($n = 3$) pressure perturbation amplitudes along parabola surface. The solution is obtained by the third-, fifth-, seventh-, and ninth-order schemes using 51×91 grid.

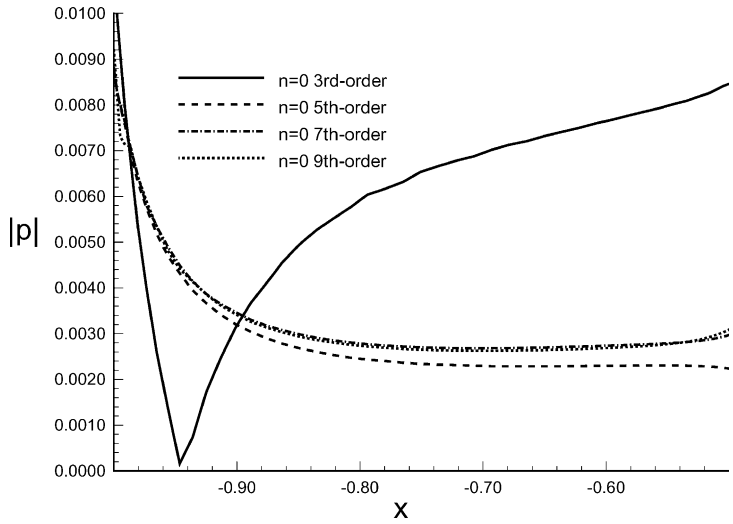

Fig. 26. Mean flow distortion ($n = 0$) for pressure perturbation amplitudes along parabola surface. The solution is obtained by the third, fifth, seventh, and ninth-order schemes using 51×91 grid.

relatively coarse 31×51 grid. Fig. 27 shows the Fourier amplitudes of pressure perturbation along the parabola surface for the same case. The solution is obtained by the ninth-order scheme using a 31×51 grid. The results show that the high-order schemes capture the fundamental mode very well, but cannot capture the higher harmonics accurately because of the coarser grid.

Overall, the results show that with new method high order (upto 11th-order shown) computations can be carried out without any numerical problems. The scheme is completely flexible from the point of view of

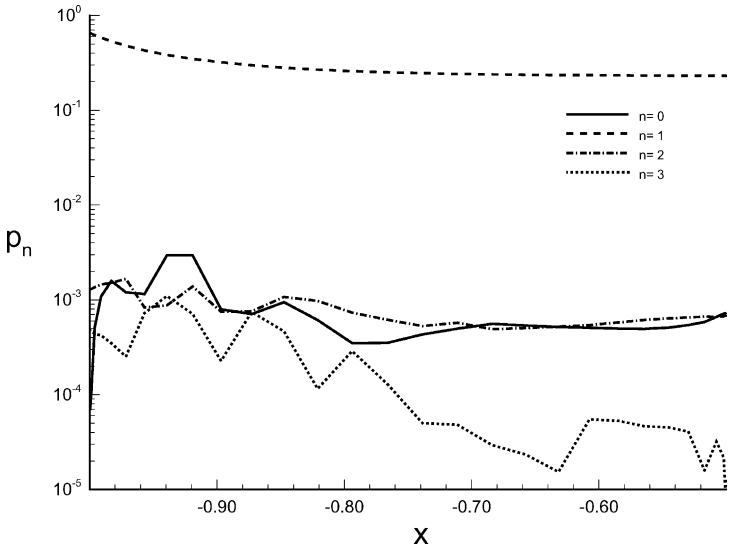

Fig. 27. Fourier amplitudes pressure perturbation along parabola surface. The solution is obtained by the ninth-order schemes using the coarser 31×51 grid.

stencil width and order of accuracy. Hence, based on the resolution requirements of the problem the most efficient stencil width can be chosen. In this paper we have shown only simple single domain computations. However, conceptually no problems are anticipated in extending the schemes to multi-domain problems following the approach of Kopriva [33] for multi-domain spectral methods.

7. Conclusion

A set of high-order schemes (upto 15th-order) with stable boundary closures, of the same order as the interior, has been derived. The schemes are asymptotically stable for linear equations. The new schemes are tested for nonlinear equations using numerical simulations of incompressible and compressible Navier–Stokes test cases. The high-order non-uniform grid schemes have been applied to 2-D hypersonic flow simulations using the nonlinear Navier–Stokes equations. Stable numerical solutions have been obtained for the receptivity of Mach 15 flow over a parabola. The accuracy of both steady and unsteady solutions obtained by using different orders of the schemes and different grid resolutions have been evaluated. The results show the new non-uniform grid schemes are stable and are able to produce highly accurate results.

Appendix A

The spatial discretization using an explicit scheme can be written in the matrix form given by Eq. (32). An example of derivative $\boldsymbol{A}$ in Eq. (32) for a 15 point domain (with $\alpha = 0.91$) and a sixth-order scheme using seven grid stencil in both interior and in boundary points is given in the matrix below. The numbers below are truncated to three significants as a demonstration, the actual significant digits of the coefficients are longer with about 15 digits for double precision calculations and can be longer if necessary.

$$A=\begin{bmatrix}
-36.368 & 45.503 & -12.961 & 5.316 & -1.887 & 0.448 & -0.051 & \cdot & \cdot & \cdot & \cdot & \cdot & \cdot & \cdot & 0 \\
-10.592 & 4.043 & 8.758 & -3.011 & 1.008 & -0.233 & 0.026 & & & & & & & & \cdot \\
3.042 & -8.831 & 1.570 & 5.340 & -1.379 & 0.288 & -0.030 & & & & & & & & \cdot \\
-1.988 & 4.836 & -8.508 & 2.824 & 3.309 & -0.524 & 0.050 & & & & & & & & \cdot \\
\cdot & -0.291 & 1.566 & -5.532 & 1.062 & 3.812 & -0.689 & 0.071 & & & & & & & \cdot \\
\cdot & & -0.152 & 1.099 & -4.731 & 0.462 & 4.008 & -0.769 & 0.083 & & & & & & \cdot \\
\cdot & & & -0.116 & 0.943 & -4.403 & 0.183 & 4.121 & -0.819 & 0.092 & & & & & \cdot \\
\cdot & & & & -0.101 & 0.869 & -4.233 & 0.000 & 4.233 & -0.869 & 0.101 & & & & \cdot \\
\cdot & & & & & -0.092 & 0.819 & -4.121 & -0.183 & 4.403 & -0.943 & 0.116 & & & \cdot \\
\cdot & & & & & & -0.083 & 0.769 & -4.008 & -0.462 & 4.731 & -1.099 & 0.152 & & \cdot \\
\cdot & & & & & & & -0.071 & 0.689 & -3.812 & -1.062 & 5.532 & -1.566 & 0.291 & \cdot \\
\cdot & & & & & & & & -0.050 & 0.524 & -3.309 & -2.824 & 8.508 & -4.836 & 1.988 \\
\cdot & & & & & & & & 0.030 & -0.288 & 1.379 & -5.340 & -1.570 & 8.831 & -3.042 \\
\cdot & & & & & & & & -0.026 & 0.233 & -1.008 & 3.011 & -8.758 & -4.043 & 10.592 \\
0 & \cdot & \cdot & \cdot & \cdot & \cdot & \cdot & \cdot & 0.051 & -0.448 & 1.887 & -5.316 & 12.961 & -45.503 & 36.368
\end{bmatrix}. \tag{A.1}$$

The spatial discretization using a compact scheme can be written in matrix form given by Eq. (47). An example of the coefficient matrices $\boldsymbol{P}$ and $\boldsymbol{Q}$ for a 7–3 compact scheme for a 15 point domain (with $\alpha = 0.8$) is given below:

$$P=\begin{bmatrix}
1.000 & 0.223 & -0.066 & \cdot & \cdot & \cdot & \cdot & \cdot & \cdot & \cdot & \cdot & \cdot & \cdot & \cdot & 0 \\
0.046 & 1.000 & 0.343 & & & & & & & & & & & & \cdot \\
\cdot & 0.615 & 1.000 & 0.340 & & & & & & & & & & & \cdot \\
\cdot & & 0.791 & 1.000 & 0.251 & & & & & & & & & & \cdot \\
\cdot & & & 0.519 & 1.000 & 0.306 & & & & & & & & & \cdot \\
\cdot & & & & 0.439 & 1.000 & 0.339 & & & & & & & & \cdot \\
\cdot & & & & & 0.402 & 1.000 & 0.361 & & & & & & & \cdot \\
\cdot & & & & & & 0.380 & 1.000 & 0.380 & & & & & & \cdot \\
\cdot & & & & & & & 0.361 & 1.000 & 0.402 & & & & & \cdot \\
\cdot & & & & & & & & 0.339 & 1.000 & 0.439 & & & & \cdot \\
\cdot & & & & & & & & & 0.306 & 1.000 & 0.519 & & & \cdot \\
\cdot & & & & & & & & & & 0.251 & 1.000 & 0.791 & & \cdot \\
\cdot & & & & & & & & & & & 0.340 & 1.000 & 0.615 & \cdot \\
\cdot & & & & & & & & & & & & 0.343 & 1.000 & 0.046 \\
0 & \cdot & \cdot & \cdot & \cdot & \cdot & \cdot & \cdot & \cdot & \cdot & \cdot & \cdot & -0.066 & 0.223 & 1.000
\end{bmatrix}, \tag{A.2}$$

$$Q=\begin{bmatrix}
-44.750 & 49.766 & -5.503 & 0.524 & -0.040 & 0.004 & -0.0002 & \cdot & \cdot & \cdot & \cdot & \cdot & \cdot & \cdot & 0 \\
-16.392 & 8.256 & 7.948 & 0.203 & -0.016 & 0.001 & -0.0001 & & & & & & & & \cdot \\
-6.887 & -2.559 & 3.923 & 5.335 & 0.199 & -0.012 & 0.0005 & & & & & & & & \cdot \\
1.469 & -4.748 & -4.831 & 4.308 & 3.705 & 0.100 & -0.003 & & & & & & & & \cdot \\
\cdot & 0.104 & -0.949 & -4.972 & 1.804 & 3.857 & 0.162 & -0.006 & & & & & & & \cdot \\
\cdot & & 0.034 & -0.491 & -4.483 & 0.837 & 3.906 & 0.206 & -0.008 & & & & & & \cdot \\
\cdot & & & 0.019 & -0.349 & -4.196 & 0.341 & 3.952 & 0.243 & -0.010 & & & & & \cdot \\
\cdot & & & & 0.013 & -0.284 & -4.037 & 0.000 & 4.037 & 0.284 & -0.013 & & & & \cdot \\
\cdot & & & & & 0.010 & -0.243 & -3.952 & -0.341 & 4.196 & 0.349 & -0.019 & & & \cdot \\
\cdot & & & & & & 0.008 & -0.206 & -3.906 & -0.837 & 4.483 & 0.491 & -0.034 & & \cdot \\
\cdot & & & & & & & 0.006 & -0.162 & -3.857 & -1.804 & 4.972 & 0.949 & -0.104 & \cdot \\
\cdot & & & & & & & & 0.003 & -0.100 & -3.705 & -4.308 & 4.831 & 4.748 & -1.469 \\
\cdot & & & & & & & & -0.0005 & 0.012 & -0.199 & -5.335 & -3.923 & 2.559 & 6.887 \\
\cdot & & & & & & & & 0.0001 & -0.001 & 0.016 & -0.203 & -7.948 & -8.256 & 16.392 \\
0 & \cdot & \cdot & \cdot & \cdot & \cdot & \cdot & \cdot & 0.0002 & -0.004 & 0.040 & -0.524 & 5.503 & -49.766 & 44.750
\end{bmatrix}. \tag{A.3}$$

References

[1] Defense Science Board, Final Report of the Second Defense Science Board Task Force on the National Aero-space Plane (NASP), AD-A274530, 94-00052, November, 1992.

[2] Th. Herbert, M.V. Morkovin, Dialogue on bridging some gaps in stability and transition research, in: R. Eppler, H. Fasel (Eds.), Laminar-Turbulent Transition, IUTAM Symposium, Stuttgart, Germany, Springer, Berlin, 1980, pp. 47–72.

[3] M.V. Morkovin, E. Reshotko, Dialogue on progress and issues in stability and transition research, in: D. Arnal, R. Michel (Eds.), Laminar-Turbulent Transition, IUTAM Symposium Toulouse, Springer, Berlin, 1990, pp. 3–30.

[4] E. Reshotko, Boundary layer instability, transition and control, AIAA paper 94-0001, 1996.

[5] T. Herbert, Progress in Applied Transition Analysis, AIAA Paper 96-1993, 27th AIAA Fluid Dynamics Conference, New Orleans, LA, June 1996.

[6] D. Bushnell, Notes on initial disturbance field for the transition problem, in: M.Y. Hussaini, R.G. Viogt (Eds.), Instability and Transition, vol. I, Springer, Berlin, 1990, pp. 217–232.

[7] M. Morkovin, On the many faces of transition, in: C.S. Wells (Ed.), Viscous Drag Reduction, Plenum, New York, 1969, pp. 1–31.

[8] L.M. Mack, Boundary layer linear stability theory, In AGARD Report, No. 709, 1984, pp. 3-1–3-81.

[9] M.V. Morkovin, Transition at hypersonic speeds, ICASE Interim Report 1, NASA CR 178315, May, 1987.

[10] D. Arnal, Laminar-turbulent transition problems in supersonic and hypersonic flows, Special Course on Aerothermodynamics of Hypersonic Vehicles, AGARD Report No. 761, 1988.

[11] E. Reshotko, Hypersonic stability and transition, in: J.-A. Desideri, R. Glowinski, J. Periaux (Eds.), Hypersonic Flows for Reentry Problems, vol. 1, Springer, Berlin, 1991, pp. 18–34.

[12] H.L. Reed, W.S. Saric, Stability of three-dimensional boundary layers, Ann. Rev. Fluid Mech. 21 (1989) 235–284.

[13] K.F. Stetson, R.L. Kimmel, On hypersonic boundary layer stability, AIAA paper 92-0737, 1992.

[14] S.K. Lele, Compact finite difference schemes with spectral-like resolution, J. Comput. Phys. 103 (1992) 16–42.

[15] C.D. Pruett, T.A. Zang, C.-L. Chang, M.H. Carpenter, Spatial direct numerical simulation of high-speed boundary-layer flows. part I: Algorithmic considerations and validation, Theor. Comput. Fluid Dyn. 7 (1995) 49–76.

[16] N.A. Adams, Subharmonic transition to turbulence in a flat-plate boundary layer at mach number 4.5, J. Fluid Mech. 317 (1996) 301–335.

[17] K. Mahesh, A family of high order finite difference schemes with good spectral resolution, J. Comput. Phys. 145 (1998) 332–358.

[18] D.V. Gaitonde, M.R. Visbal, Further development of a Navier–Stokes solution procedure based on higher-order formulas, AIAA paper 99-0557, 1999.

[19] X. Zhong, High-order finite-difference schemes for numerical simulation of hypersonic boundary-layer transition, J. Comput. Phys. 144 (1998) 662–709.

[20] X. Zhong, Leading-edge receptivity to free stream disturbance waves for hypersonic flow over a parabola, J. Fluid Mech. 441 (2001) 315–367.

[21] M.M. Rai, P. Moin, Direct numerical simulation of transition and turbulence in a spatially evolving boundary layer, J. Comput. Phys. 109 (1993) 169–192.

[22] D.W. Zingg, H. Lomax, H. Jurgens, High-accuracy finite-difference schemes for linear wave propagation, SIAM J. Sci. Comput. 17 (2) (1995) 328–346.

[23] N.A. Adams, K. Shariff, A high-resolution hybrid compact-eno scheme for shock–turbulence interaction problems, J. Comput. Phys. 127 (1996) 27–51.

[24] M.H. Carpenter, D. Gotlieb, S. Abarbanel, The stability of numerical boundary treatments for compact high-order finite-difference schemes, J. Comput. Phys. 108 (1993) 272–295.

[25] S.S. Abarbanel, A.E. Chertock, A. Yefet, Strict stability of high-order compact implicit finite-difference schemes: the role of boundary conditions for hyperbolic PDEs, I, J. Comput. Phys. 160 (2000) 42–66.

[26] H.O. Kreiss, G. Scherer, Finite element and finite difference methods for hyperbolic partial differential equations, Math. Aspect Finite Elem Partial Diff Equations (1974).

[27] B. Strand, Summation by parts for finite difference approximations for d/dx, J. Comput. Phys. 110 (1994) 47–67.

[28] D.A. Kopriva, Spectral solution of the viscous blunt body problem, AIAA J. 31 (7) (1993) 1235–1242.

[29] D. Kosloff, H. Tal-Ezer, A modified Chebyshev pseudospectral method with an $O(1/N)$ time step restriction, J. Comput. Phys. 104 (1993) 457–469.

[30] C. Canuto, M.Y. Hussaini, A. Quarteroni, T.A. Zang, Spectral Methods in Fluid Mechanics, Springer, New York, 1988.

[31] H. Fasel, Investigation of the stability of boundary layers by a finite difference model of the Navier–Stokes equations, J. Fluid Mech. 78 (1976) 355–383.

[32] X. Zhong, Direct numerical simulation of hypersonic boundary-layer transition over blunt leading edges, Part II: Receptivity to sound (Invited), AIAA paper 97-0756, January 1997.
[33] D.A. Kopriva, Multidomain spectral solutions of high-speed flows over blunt cones, AIAA J. 31 (12) (1993).